frontiers | Frontiers in Earth Science

TYPE Original Research
PUBLISHED 12 September 2024
DOI 10.3389/feart.2024.1456055

Check for updates

OPEN ACCESS

EDITED BY
Kun Shi,
Chinese Academy of Sciences (CAS), China

REVIEWED BY
Abdelazim Negm,
Faculty of Engineering, Zagazig University, Egypt
Mohamed Abioui,
Ibn Zohr University, Morocco

*CORRESPONDENCE
Mostafa Nagy,
mostafa_fadila@sci.kfs.edu.eg
Tamer Abu-Alam,
tamer.abu-alam@uit.no

RECEIVED 27 June 2024
ACCEPTED 29 August 2024
PUBLISHED 12 September 2024

CITATION
El-Badrawy HT, Abbas AM, Massoud U, Abu-Alam T, Alrefaee HA, Abo Khashaba SM and Nagy M (2024) Integrated approach-based groundwater mapping in sohag governorate, upper Egypt, using remote sensing and aeromagnetic data. *Front. Earth Sci.* 12:1456055. doi: 10.3389/feart.2024.1456055

COPYRIGHT
© 2024 El-Badrawy, Abbas, Massoud, Abu-Alam, Alrefaee, Abo Khashaba and Nagy. This is an open-access article distributed under the terms of the Creative Commons Attribution License (CC BY). The use, distribution or reproduction in other forums is permitted, provided the original author(s) and the copyright owner(s) are credited and that the original publication in this journal is cited, in accordance with accepted academic practice. No use, distribution or reproduction is permitted which does not comply with these terms.

Integrated approach-based groundwater mapping in sohag governorate, upper Egypt, using remote sensing and aeromagnetic data

Hussein T. El-Badrawy[1], Abbas M. Abbas[2], Usama Massoud[2], Tamer Abu-Alam[3,4,5]*, Hamed A. Alrefaee[1], Saif M. Abo Khashaba[1] and Mostafa Nagy[1]*

[1]Geology Department, Faculty of Science, Kafr Elsheikh University, Kafr Elsheikh, Egypt, [2]National Research Institute of Astronomy and Geophysics (NRIAG), Helwan, Cairo, Egypt, [3]The Faculty of Biosciences, Fisheries and Economics, UiT The Arctic University of Norway, Tromsø, Tromsø, Norway, [4]OSEAN—Outermost Regions Sustainable Ecosystem for Entrepreneurship and Innovation, Colégio dos Jesuítas, University of Madeira, Funchal, Portugal, [5]Research Department, CloudEARTHi AS, Tromsø, Norway

Introduction: Groundwater demand has been considerably heightened due to rapid urban growth, specifically in arid areas that rely primarily on groundwater. This study aims to utilize remote sensing and aeromagnetic data, combined with the Analytic Hierarchy Process (AHP) based GIS, to evaluate potential groundwater zones in the Sohag area, Egypt.

Methods: Nine thematic layers, including soil moisture, rainfall, lithology, normalized difference vegetation index (NDVI), drainage density, lineament density, slope, and land use/land cover, were developed using various remote sensing datasets. Besides the remote sensing-derived thematic layers, a geophysics-derived thematic layer represented by the RTP aeromagnetic map was included. The aeromagnetic data were analyzed and interpreted to outline the subsurface structure affecting groundwater storage and flow. Also, the aeromagnetic data analysis helps estimate the basement depth that constitutes the Nubian Aquifer's base and identifies regions with considerable thick sedimentary deposits and significant water reserves.

Results and discussion: The groundwater potentiality map was consistent with production wells in the area, and sites for drilling new wells were predicted, especially in the Nile Valley around the Tahta, El-Hamimia, and west Sohag cities. The most promising sites are clustered along the Nile Valley, and the study area's northwestern and northeastern parts. The results indicate that the predominant magnetic structural trends are NW-SE, NE-SW, N-S, and E-W, which contribute to the formation of a series of subsurface horsts (H) and grabens (G). Three main basins (A, B, and C) were identified as the most profound areas. These basins represent the most promising areas for groundwater accumulation,

making them attractive for future hydrogeological exploration. This integrated approach strongly offers a powerful and effective tool to assist in developing an appropriate plan to manage groundwater in arid regions.

KEYWORDS

remote sensing, radar data, aeromagnetic, groundwater potentiality, Sohag

1 Introduction

Water is indispensable for sustaining human life and agricultural, urban, and industrial development. Egypt is a country in the northeast of Africa and experiences arid desert conditions characterized by low rainfall. There is a shortage of surface freshwater. The principal source of surface freshwater is the Nile River, which crosses from the South to the North. Groundwater is considered an essential water source as a result of rapid population expansion, increased human activity, and decreased *per capita* share of different water supplies. Especially in Egypt, the future of freshwater is far from optimistic because of the impact of climate change and Ethiopia's Renaissance Dam construction, which will degrade freshwater supplies from the Nile River. Groundwater demand has increased due to the challenges mentioned above. Groundwater potential can be thoroughly evaluated by delineating the recharge sources, whether surface water infiltrating or migrating from near aquifers through structural systems. Several authors have highlighted the area around Sohag as a significant area of economic potential (Mahmoud and Kotb, 2017; Ghazala et al., 2018a; Ibraheem et al., 2019; Elbeih et al., 2021). Egypt's government has recommended that the study area become a part of several national projects across several sectors, such as agriculture, industry, and housing.

Recently, remote sensing data has been proven effective in delineating high-potential groundwater areas utilizing various multi-criteria decision-making methods such as the Analytic Hierarchy Process (AHP) (Meijerink et al., 2007; Patra et al., 2016; Shebl et al., 2021; Melese and Belay, 2022; Shebl et al., 2022). The Analytic Hierarchy Process (AHP) is a widely recognized decision-making technique that integrates subjective judgments and multiple evaluation factors to complement the decision-making process. By following this systematic AHP-based approach, researchers and decision-makers can effectively combine quantitative data and subjective expert opinions to delineate groundwater potential areas, supporting more informed groundwater management and exploration strategies (Wind and Saaty, 1980; Das et al., 2017; Mukherjee and Singh, 2020; Al-Djazouli et al., 2021; Dar et al., 2021; Shebl et al., 2022; Ikirri et al., 2023; Ally et al., 2024).

Through the analysis and interpretation of remote sensing images, it is possible to map and investigate the surface elements that affect runoff penetration, such as geological settings, drainage networks, soil cover, and climate. These elements essentially represent the hidden subsurface hydrogeological parameters, like groundwater recharge, accumulation, and storage capacity (Meijerink et al., 2007; Gaber et al., 2020). Groundwater potential zones can be better defined by studying the influence of these factors as well as aeromagnetic data (Meijerink et al., 2007; Arunbose et al., 2021). Magnetic data can effectively explore groundwater resources, particularly in large or inaccessible areas where preliminary geophysical studies are needed (Araffa et al., 2020; Meneisy and Al Deep, 2021; Araffa et al., 2023). In recent years, the potentiality of groundwater resources has been investigated more efficiently by integrating aeromagnetic and remote sensing methods (Meneisy, 2020; Abuzied and Alrefaee, 2017; ALDeep et al., 2021).

Groundwater exploration in vast areas can be challenging using only field data. Therefore, integrating remote sensing and aeromagnetic data is particularly useful for identifying suitable areas for further field-based groundwater assessment across extensive regions. This study aims to provide insights into the most appropriate groundwater reserve location by mapping groundwater occurrences and recharge sources. Also, this study discusses integrating remote sensing and aeromagnetic data to detect surface and subsurface structures affecting groundwater accumulations. Moreover, radar data (e.g., DEM and Sentinel-1), along with soil moisture, the Global Land Cover Map (GLCM) from Esri, rainfall data, and an updated lithological map integrated with magnetic data, were used to delineate groundwater potential zones.

2 Materials and methods

Figure 1 presents the detailed methodology of the study which have been used to achieve the study's objectives.

2.1 Study area

2.1.1 Geological and hydrological settings

The study area is predominantly located in Upper Egypt, stretching along the Nile Valley. It is bordered by latitudes 26° 00′ to 27° 00′N and longitudes 31° 00′ to 32° 00′E (Figure 2). Geomorphologically, the study area is composed of three main units: the limestone plateau, the old alluvial terraces, and the recent alluvial plain (Said, 1962). The Nile Valley is bordered by both eastern and western plateaus. The western plateau, which comprises the majority of the area under investigation compared with the eastern one, reaches an elevation of 250–350 m with surface lineaments trend NW-SE, whereas the eastern plateau is highly faulted, and its elevation ranges from 350 to 500 m. The hydro-geomorphologic features of the drainage basins cut through the Eocene plateaus and drain directly toward the Nile Valley, revealing potential sources of recharge from the Nile Valley and downward drainage into the underlying aquifer.

Geologically, the study area is characterized by sedimentary sequences extending from the Eocene to the Quaternary age (Conoco, 1987; Seif, 2015), as shown in Figure 2B. According to

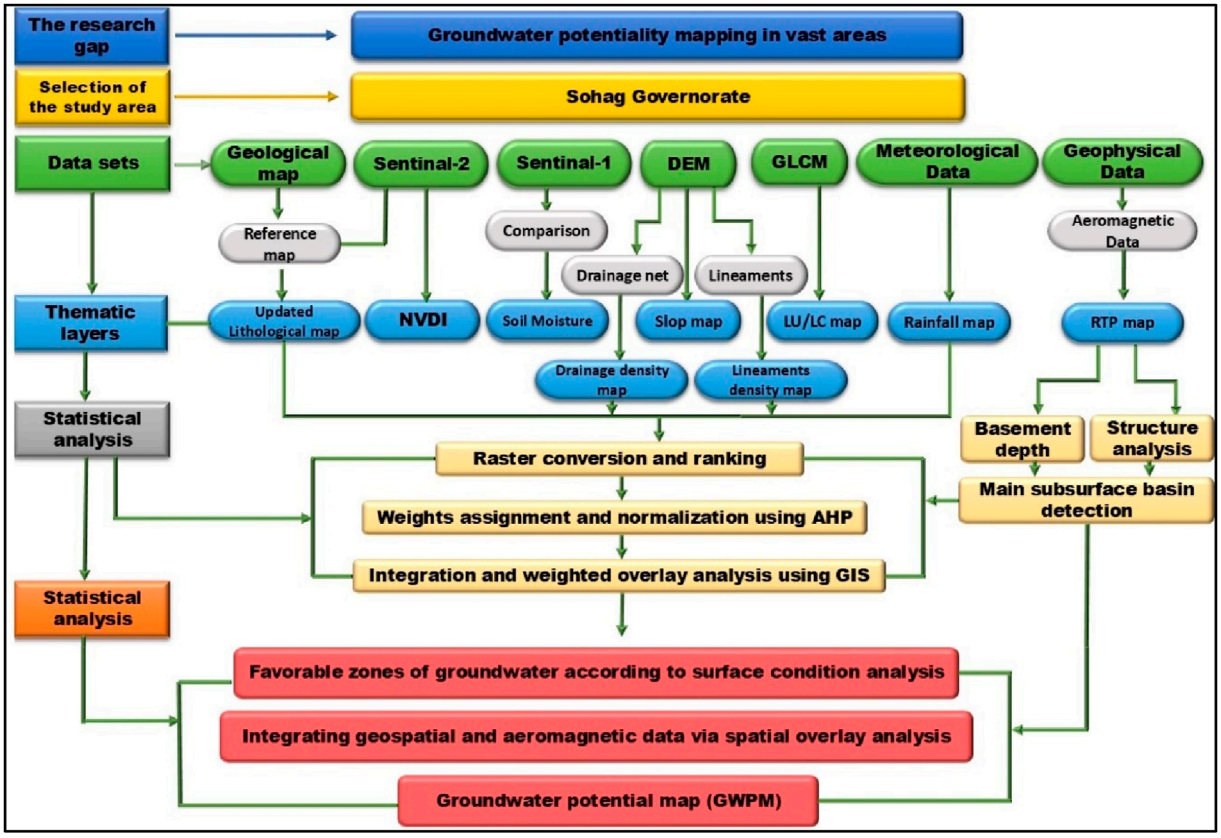

FIGURE 1
Flow chart for the detailed methodology of the study.

Abd El Aal et al. (2020), several drainage basins discharge towards the Nile Valley from east to west, bordered by the lower Eocene limestone plateau (Said, 1962). The Thebes Formation represents the Lower Eocene as a succession of massive to laminated limestone with bands of chert and marl (Mahran et al., 2013). Thebes Formation underlies the Drunka Formation, consisting primarily of thick-bedded, chalky limestone interbedded with massive limestone and includes chert bands and concretions (McBride et al., 1999). Issawia Formation is composed of lacustrine sediments in two different facies (clastic and carbonate facies) of the Pliocene/Pleistocene age due to the arid conditions of this period (Omer, 1996). Issawi Formation is covered by floodplains, mainly comprised of alluvium deposits confined to the narrow Nile Valley tract. Quaternary deposits mainly consist of wadi deposits, pre-Nile sediments, playa deposits, and alluvial fanglomerates. According to the Balyana-1 well in the study area, subsurface stratigraphy consists of various sediments ranging from the Late Cretaceous (Nubian Sandstone) to the Quaternary. These sediments lie unconformably over Precambrian basement rocks at a depth of approximately 1,640 m (Ganoub El-Wadi Petroleum Holding Company, 1994). The top layers consist of Quaternary sand, silt, and shale, underlain by layers comprised of shale and sandstone from the Lower Eocene age, whereas the Upper Cretaceous sandstone layers are interbedded with shale and rest on the Precambrian granitic basement rocks (Figure 2C).

Structurally, the study area is primarily situated within the stable shelf region. It is mainly affected by various faults that strike in four different trends: NW–SE (Gulf of Suez trend), NE–SW (Aqaba trend), E–W (Tethyan-Mediterranean trend), and N–S trend. Tensional forces are responsible for the structural features in the study area (Mostafa, 1979; Zaki, 2001). The Eocene plateau is affected by several normal faults (Said, 1962). Normal faulting dominated the Pre-Tertiary structural pattern within the Western Desert region, forming horst and graben structures as well as drag folds (Sestini, 1984). Lowlands (floodplains) developed as grabens by upthrowing plateaus on the Nile River's eastern and western sides (Youssef, 1968).

Hydrogeologically, the study area's surface water sources include the Nile River, its tributaries, and irrigation channels, whereas the Pleistocene Eocene aquifers are the primary groundwater sources in the study area (Abdel Moneim, 1988; Omran et al., 2006; Mahmoud and Kotb, 2017). The Pleistocene Aquifer comprises gravel and graded sands covered by semi-permeable alluvial deposits and rests on an impermeable Pliocene clay deposit (Figure 2D). The groundwater occurrence around the Nile Valley is semi-confined, whereas it is unconfined along the desert fringes due to the absence of the Nile silt layer. The thickness, width, and geometry of the aquifer vary between different locations (Attia, 1974; Farrag, 1982). Along the River Nile, the Pleistocene aquifer has a thickness of approximately 260 m and decreases toward the Eocene plateau

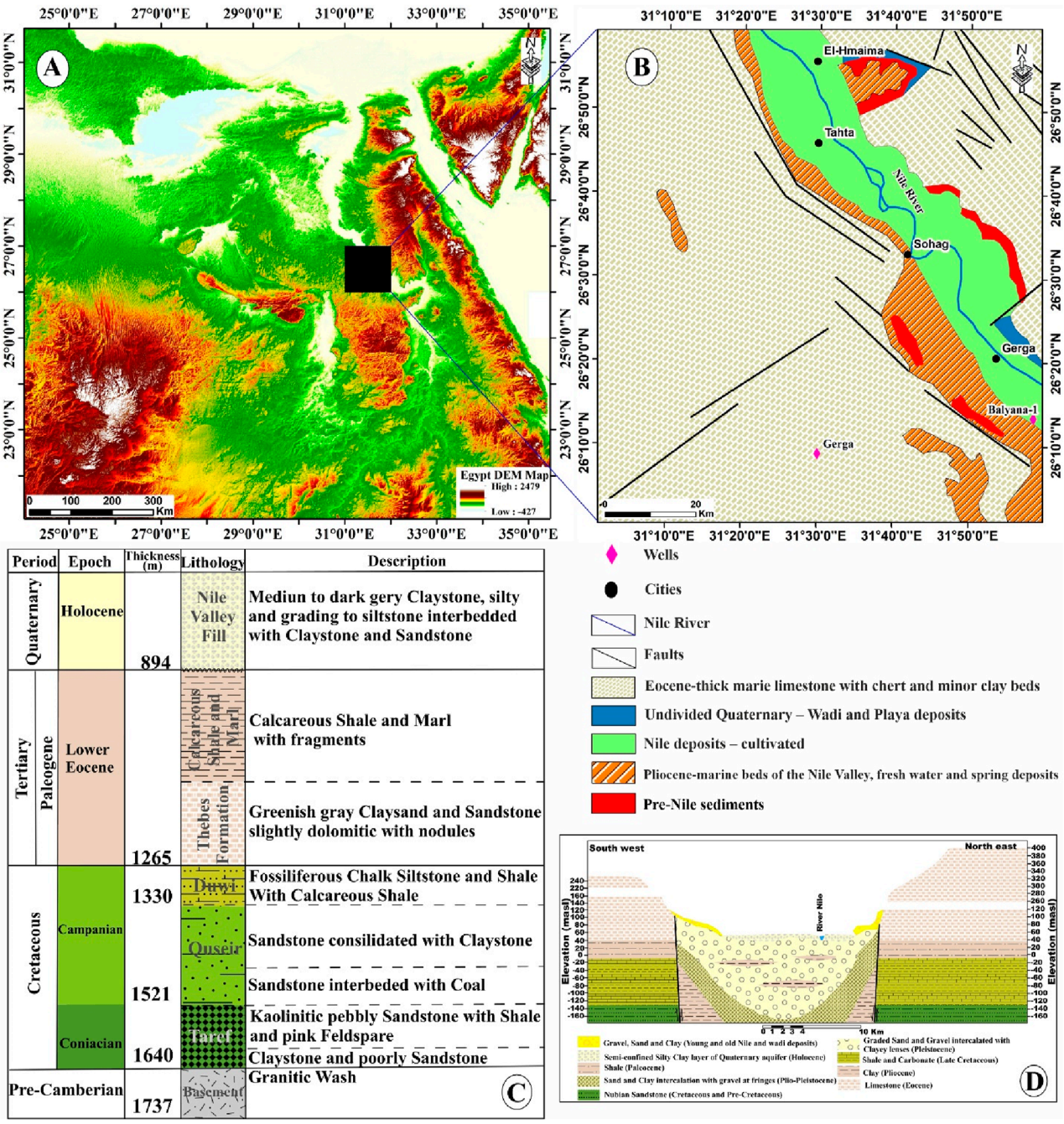

FIGURE 2
(A) Digital elevation model (DEM) of Egypt. **(B)** Geologic map of the Sohag area (modified after EGSMA, 1981). **(C)** The stratigraphic column for the Balyana-1 well (after Ganoub El-Wadi Petroleum Holding Company, 1994). **(D)** The general hydrogeological cross-section of the Sohag area (after RIGW, 1997).

(Abu El Magd, 2008). The Eocene Aquifer comprises fractured limestone, with semi-confined to confined groundwater conditions (El Sabri, 2011). Among the study area's aquifers, Nubian Sandstone is the deepest. The series of Nubian Sandstones is the major aquifer in North Africa, not just the Western Desert of Egypt (Diab, 1972). According to RIGW (2023), The study area contains water levels that range from 4.87 to 200 m below the ground surface. Table 1 provides information about the selected wells.

2.2 Remote sensing data

The Sohag area was analyzed using remote sensing imagery and GIS analysis to identify potential groundwater zones. The remotely sensed data include Radar data such as Sentinel-1B (C-band synthetic aperture radar (SAR)) and Shuttle Radar Topography Mission (SRTM) Digital Elevation Model (DEM) (Figure 1). Sentinel-1B radar data was used to delineate the surface structure lineaments

TABLE 1 A summary of the selected wells' results after RIGW (2023).

Well	Latitude	Longitude	Water table (m)	Maximum depth (m)	Water bearing formation (aquifer)	TDS (ppm)
West El Balyana-1	26° 13′03″	31° 41′39″	200	280	Eocene limestone	1849
West El Balyana-2	26° 14′20″	31° 48′01″	90	150	Eocene limestone	1,166
Gerga	26° 20′22″	31° 53′16″	5.10	38	Pleistocene sands	1,340
El Minshah	26° 28′54″	31° 47′47″	4.87	44	Pleistocene sands	1,570
El Maraghah	26° 42′00″	31° 35′59″	6.20	44	Pleistocene sands	1,270
Tahta	26° 46′00″	31° 30′18″	6.15	45	Pleistocene sands	980
West Tahta-1	26° 43′10″	31° 24′16″	23.72	32	Pleistocene sands	1,242
West Tahta-2	26° 42′09″	31° 25′39″	14.62	67	Pleistocene sands	1,381

in the area under study. Sentinel-1B data (S1B_IW_GRDH_1SDV_20210908T155515_20210908T155540_028609_0369FD_877A) was acquired on 8 September 2021. The LINE extraction algorithm in a Geomatica-PCI software was utilized for automatic lineament extraction, which involved extracting the lineament's predominant directions from a Sentinel-1 radar image.

Additionally, the rose diagram was created using the Rockwork version 2018 software. The lineament density has been developed based on ArcGIS software version 10.8 to calculate the lineament frequency per unit area (number/km^2) applied to Sentinel-1B data. The Digital Elevation Model (DEM) data, sourced freely from the USGS website, has a spatial resolution of 30 m. It was utilized to derive structural surface elevation, compute slope, and delineate various watersheds along with their associated drainage networks using ArcGIS version 10.8 software.

Sentinel-2 data were employed to compute the Normalized Difference Vegetation Index (NDVI) and Moisture Index (Figure 1). The preprocessing of Sentinel-2 data involved georeferencing and radiometric correction using the Sentinel Application Platform (SNAP). Furthermore, a 10 m Land Use/Land Cover map (LU/LC) was created using Esri's recently published Global Land Cover Map (GLCM), which also relies on Sentinel 2 data. All remotely sensed datasets have been geometrically adjusted to the Universal Transverse Mercator (UTM), Zone 36 North projection, using the WGS-84 datum.

2.3 Aeromagnetic data

The RTP aeromagnetic data were digitized from the Upper Nile Valley aeromagnetic sheet owned by (Aero Service Division of the Egyptian Nile Valley Petroleum Company, 1993). The aeromagnetic map scale is 1:250,000, and its contour interval is 5 nT. The aeromagnetic map is mainly utilized to assess the basement depth, outline the basement rock architecture, and delineate subsurface faults in the study area to provide a holistic grasp of the hydrogeological setting. Regional effects on the Earth's magnetic field were eliminated by removing the IGRF values. The Fast Fourier Transform was used to reduce the collected magnetic data to the magnetic north pole (RTP) to avoid the shift and undesirable distortions in the locations, shapes, and sizes of magnetic anomalies (Baranov, 1964).

2.3.1 Regional-residual separation

The RTP map exhibits multiple anomalies, which can be attributed to a variety of sources. These consist of residual anomalies, distinguished by their short wavelengths and originating from shallow and small sources, and regional anomalies, characterized by long wavelengths and attributed to deep and large sources (Lowrie, 2007). In general, anomalies separation involves processing methods that aim to separate the effects of shallow from deep sources. Blakely (1996) suggested that High-pass filters amplify residual anomalies while low-pass filters amplify regional anomalies. Filters with a cut-off wavenumber of 0.025 (radian/km) were applied to the RTP map to isolate and enhance residual and regional anomalies, respectively.

Two main magnetic data analysis procedures were utilized to support groundwater investigations (Figure 1). First, the structure analysis is applied to traditional techniques (RTP, residual, and regional magnetic maps) and high-precision edge detection techniques (ETILT, ETHDR, STDR, THDR-STDR, impTDX, THDR-impTDX) to delineate the main structure trends and faults' locations. This procedure is vital in groundwater studies to detect subsurface water flow direction. Many authors have applied similar techniques (Araffa et al., 2018; Nasuti et al., 2019; Pham et al., 2023; Ibraheem et al., 2023; Othman and Ibraheem, 2024). The second procedure uses the source parameter imaging (SPI) technique and 2-D magnetic modelling, which entails estimating the basement depth to define the Nubian aquifer base in the study area and to locate areas with significant, thick sedimentary cover and substantial water reserves.

2.3.2 High-precision edge detection

Magnetic source edge detection is crucial for subsurface geologic interpretations of magnetic data. Recently, various edge detectors have been extensively applied to highlight geologic structures such as faults, contacts, and dykes (Pham et al., 2018; Ibraheem et al., 2022).

In geological terms, these edges are mapped as geological contacts whose boundaries define similar lithologies (Jorge et al., 2023). With the development of new high-precision magnetic data filters, it is ideal for integrating them in geological structure mapping. In this context, six improved techniques have been selected and applied to the data to map magnetic boundaries.

The horizontal gradient method exhibits low sensitivity to noise and is capable of detecting both shallow and deep structures (Phillips, 2002). Arisoy and Dikmen (2013) introduced a novel technique titled the enhanced total horizontal gradient of the tilt angle (ETHDR), utilizing the horizontal gradient of the ETilt filter to eliminate the high amplitude dominance that prevents THDR and AS filters from being sensitive to detecting anomalies with a wide variety of amplitudes. As with the vertical derivative, this technique highlights subtle anomalies as zero contours indicating edges of magnetic sources. Even with several adjacent magnetic sources, this filter delineates the edges of shallow and deep causative bodies more precisely than others. The ETilt filter was computed following the methodology of Arisoy and Dikmen (2013).

Nasuti et al. (2019) developed the STDR filter to overcome the diffusion challenge of the estimated edges, estimate the edges with high sharpness and accuracy, and, more specifically, separate adjacent causative bodies. This filter outlines positive and negative anomalies based on the maximum and minimum values. Additionally, this filter displays anomaly shapes. Nasuti et al. (2019) also presented the calculation of the THDR-STDR filter, which utilizes both the second vertical derivative and gradient of amplitude to detect sharper edges. In this instance, the maxima are mapped along the source boundaries. The STDR and THDR-STDR filters were calculated using the Nasuti et al. (2019) formula.

Ibraheem et al. (2023) introduced the improved horizontal tilt angle (impTDX) filter to optimize and enhance the detection of source boundaries. The filter normalizes second-order vertical derivatives (SVD) through the use of the hyperbolic tangent function. Compared with other filters, this filter exhibits sharply defined boundaries at different depths, improves the discernment of neighboring anomalies, avoids false edges, and has lower sensitivity to noise. The impTDX filter response varies from −1 to 1 and presents maxima above the entire source body. Ibraheem et al. (2023) also recommend calculating the THD of the impTDX filter (THD_impTDX) to obtain the maximum values along the source edges. The impTDX and THD-impTDX filters were derived following the Ibraheem et al. (2023) formula.

2.3.3 Source parameter imaging (SPI)

Thurston and Smith (1997) introduced the SPI technique, which estimates magnetic sources' depth using step-based source models. SPI is a quantitative method that automatically calculates basement depth by computing horizontal derivatives following the least squares procedure, conducted perpendicular to the strike direction. This method provides a simple, fast, and efficient procedure to determine magnetic source depths with an accuracy of ± 20% on real data set tests (Al-Badani and Al-Wathaf, 2018). Additionally, it has the advantage of reducing interference between anomaly features by utilizing second-order derivatives. The solution grid displays edge locations, dips, depths, as well as susceptibility contrasts. In the current study, the SPI was estimated using a formula by Thurston and Smith (1997).

2.3.4 Modelling

Modelling constitutes the last step in interpreting geophysical data. This process should integrate all relevant and reliable data to support the model's constraints. (Thornbury, 1985). Modelling involves integrating information from various techniques to estimate variations in a range of physical properties over a given area, such as the distributions of magnetic susceptibility. Five (2D) magnetic models were constructed along selected profiles using the GM-SYS modelling program (Geosoft, 2018). These profiles were strategically positioned to encompass the majority of the study area and intersect the two existing boreholes (Figure 7A). The magnetic susceptibility values were derived from Dobrin and Savit (1988), Hunt et al. (1995), and Reynolds (2011). Sedimentary rocks have very low susceptibility values compared to igneous rocks and are practically assumed zero for regional studies (Lowrie, 2007).

3 Results

In this study, we seek to investigate the connection between surface geological features and waterways around the Sohag area using remote sensing data, followed by an investigation of subsurface structures using aeromagnetic data.

3.1 Remote sensing

3.1.1 Surface lineaments extraction

Lineaments encompass all linear features, including linear structures, topographical alignments, soil patterns, vegetation arrangements, and lithological alignments (Gaber et al., 2020; Shebl et al., 2022; Abo Khashaba et al., 2023). Lineament extraction is a critical tool for geological exploration, such as ore deposits and groundwater potential zones (Meijerink et al., 2007; Gaber et al., 2020; Abo Khashaba et al., 2023). The automatic lineament extraction process applied to Sentinel-1B data starts with enhancing the image and filtering to detect the specific linear features of interest, facilitating their identification and tracing (Figure 3A). Several parameters applied to the image to extract lineaments are listed in Table 2. The Filter Radius (RADI) sets the radius (in pixels) to be utilized in the edge detection filter, with smaller values detecting more intricate details and higher values minimizing noise detection. In the edge detection procedure, the Edge Gradient Threshold (GTHR) sets the threshold for changes in brightness and the lowest gradient value required to be deemed an edge. The Length Threshold (LTHR) specifies the minimum curve length (in pixels) used to map curvilinear objects, which serve as lineaments for further analysis. The Fitting Error Threshold (FTHR) determines the maximum tolerance for generating curved lineaments from an arc or line segment. A line density map was created using a line density module from ArcGIS version 10.8 using the extracted lineaments shapefile from Sentinel-1B data (Figure 3B).

Furthermore, the rose diagram, illustrating principal calculated trends, was created using this transformed shapefile in Rockwork 18 software. Figures 3A, B show the image used for Sentinel-1B, the associated lineament density map, and the rose diagram. The hillshade procedure in ArcGIS was implemented on the DEM, varying the light source azimuth angles (0°, 45°, 90°, and 135°) at

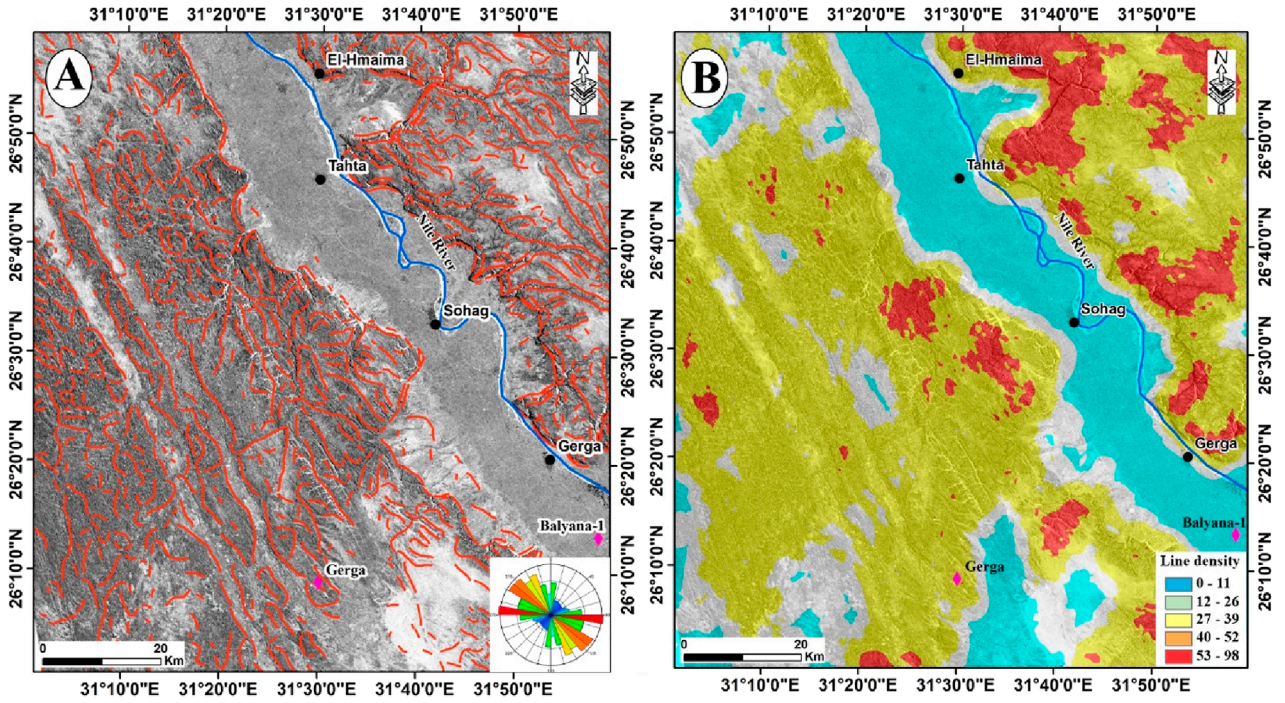

FIGURE 3
(A) Automatic lineaments extraction and rose diagram based on Sentinel-1B. **(B)** Line density map of the Sohag area.

TABLE 2 Parameters used in the lineament extraction algorithm.

Data/Parameter (B)	Radi	Gthr	Lthr	Father	Athr	Dthr
Sentinel-1	10	100	30	3	30	20

an altitude of 45° to render the terrains as shaded relief, thereby enhancing the detection of linear features (Figure 4).

The results of automatic surface structure lineaments extraction demonstrate that the prevailing direction in the area is NW-SE (Red Sea-Gulf of Suez), with minor E-W (Tethyan-Mediterranean) and N-S (Nubian) trends (Figure 3A). Most of them are constrained to Eocene limestone plateaus, while the Quaternary alluvium filling the valleys lacks lineaments (Figure 2B).

3.1.2 Groundwater recharge based on DEM

This study employed DEM data to construct and map the topography, geomorphological features, and hydrological characteristics of the study area. Furthermore, DEM data facilitate the extraction of various layers, including drainage patterns, stream orders, slopes, and basin analysis (Figure 5). The DEM reveals a decrease in elevation from 499 m on the plateau to approximately 52 m along the historic alluvial floodplain (Figure 5A). Furthermore, slope affects flow direction, groundwater recharging, and, consequently, groundwater potential (Figure 5B). Based on the slope map, the research area has gentle, moderate, and steep slopes, varying from 0° to 68.11° (Figure 5B).

Based on SRTM DEM data, drainage networks were created using the ArcGIS Hydro tool (Jenson and Dominique, 1988). The total number of stream orders was calculated based on the drainage network analysis. Subsequently, the study area was partitioned into a major basin and several smaller basins, categorized according to the dispersion and length of stream orders (Figures 5C, D). The mainstream network recharges the Nile River (Figures 2B, 5C,D), which provides the dominant recharge supply for the Nubian sandstone aquifer, depicted in black with order 5 (Figure 5C). The primary watershed, representing the basin of surface water accumulation, is delineated in yellow. It provides a clear indication of water flow direction towards the Nile River (Figure 5D). The drainage network (together with the slope) depicts the occurrence of rainfall as well as potential runoff water collection points (Ashmawy et al., 2018; Shebl et al., 2022). The drainage channels within the study area exhibit straight and parallel characteristics extending for several kilometers (Figure 5D). The resultant automatic drainage networks reveal high drainage densities in southern Sohag and northern Tahta.

3.1.3 Soil moisture, rainfall, lithology, NDVI, and LU/LC factors

Soil moisture is the most critical hydrogeology variable (Shebl et al., 2022). It was placed first in AHP because the moisture content in this arid environment strongly suggests the occurrence

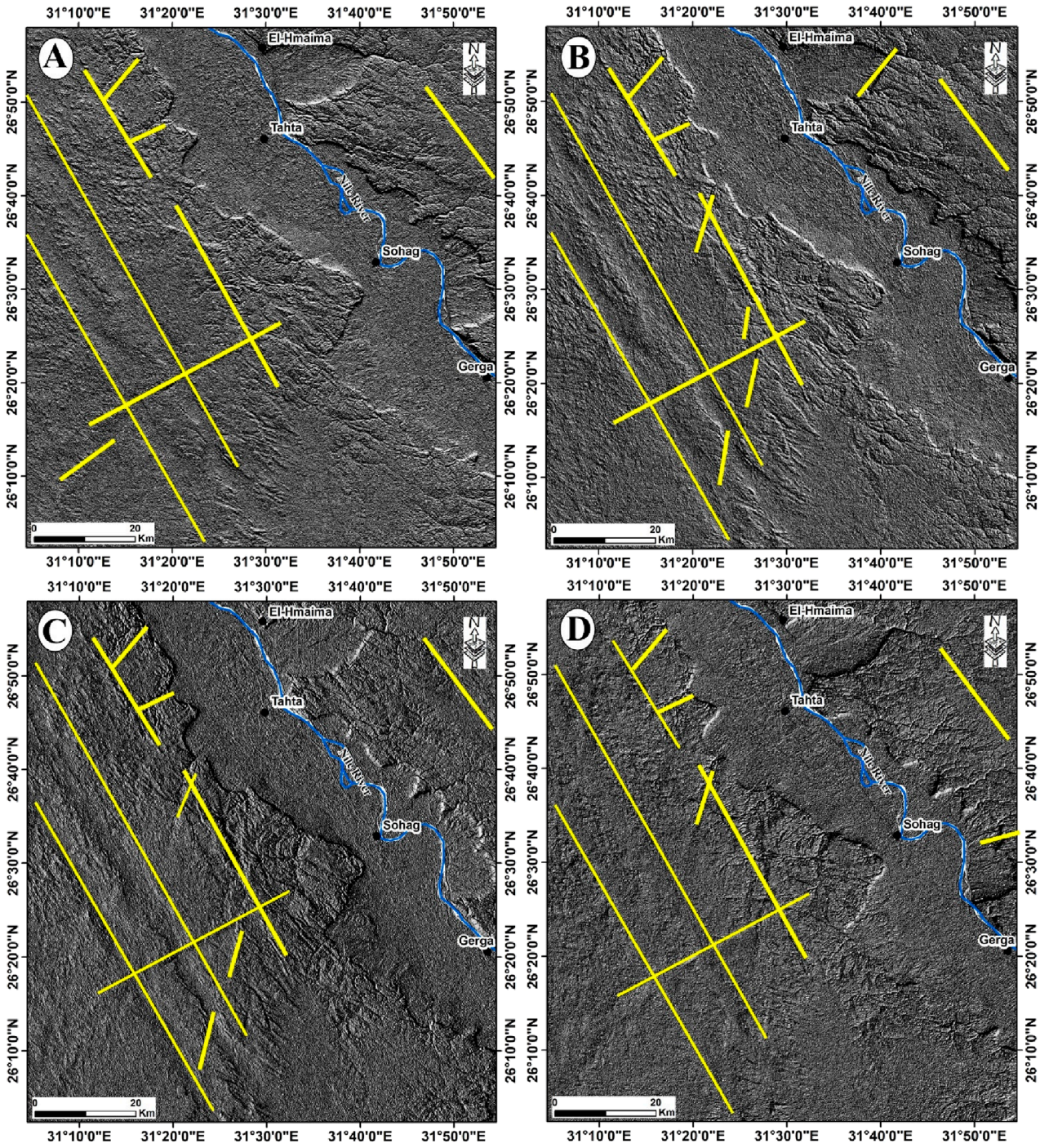

FIGURE 4
SRTM-DEM Shaded-relief image derived using a light source azimuth in different angles and an altitude of 45° **(A)** Angle 0°. **(B)** 45°. **(C)** 90°. **(D)** 135°. The yellow lines refer to the faults detected manually.

of groundwater, vegetation, or rainfall (Figure 6A). Rainfall is identified as the second most crucial component and a key hydrological source contributing to the increase in groundwater storage (Arulbalaji et al., 2019); it directly affects the amount of infiltration and storage based on exposed rock units and slope type (Figure 6B). Furthermore, the annual rainfall averages from 1998 to 2009 ranged between 0 and 159 mm (Figure 6B). The recharge rate is high in the southwest part of the study area, while it is extremely low in the rest of the study area. The recharge rate increases as rainfall increases (Gaber et al., 2020). The lithology is the third most crucial thematic layer in identifying groundwater potential zones. Rainfall is difficult to penetrate without adequate lithological units, and aquifers cannot store groundwater. To facilitate the use of the AHP tool, we categorized the geological map we generated into

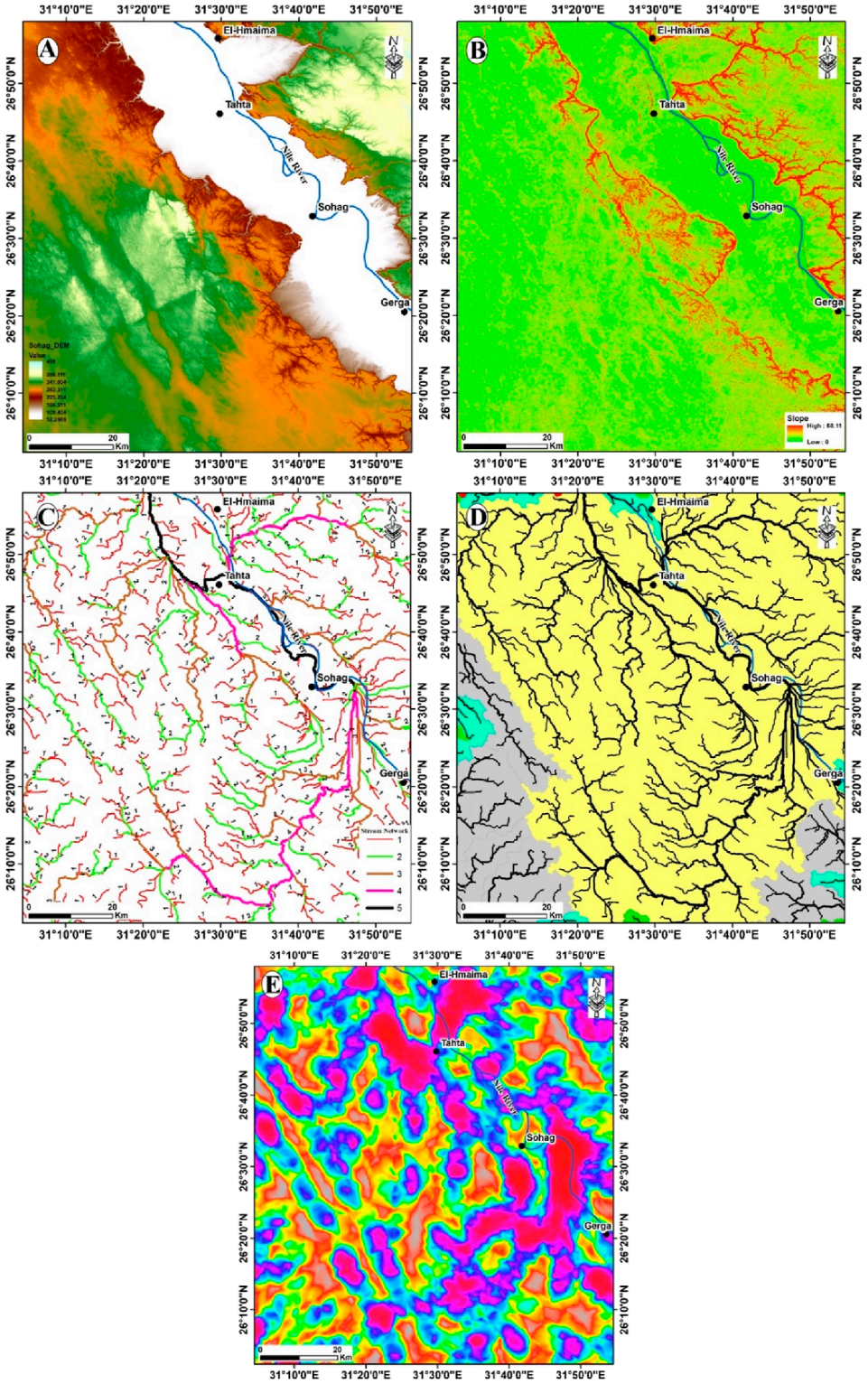

FIGURE 5
(A) SRTM digital elevation model (DEM) of the study area. **(B)** Surface slope map in degrees. **(C)** Stream order. **(D)** Watersheds and drainage channels. **(E)** Drainage density.

five primary sections, considering their hydrogeological properties (primarily permeability) as follows: 1) low (Eocene thick limestone), 2) moderate (Quaternary and playa deposits), 3) high (pre-Nile sediments), 4) very high (Pliocene marine beds), and 5) excellent (Nile deposits). NDVI is regarded as a reliable indicator of groundwater, particularly in certain areas and ecosystems. In this

work, a pixel-based NDVI range between −1.0 and +1.0 is computed to estimate groundwater potentiality and recognize land cover types using the following equation (Taloor et al., 2021) to Sentinel2 data: NDVI = (B8 + B4)/(B8 + B4). Figure 6C displays the resultant NDVI map values (−0.05–1.0), indicating dense vegetation around the Nile River, which decreases further away from the river. The produced LU/LC map of the Sohag area revealed that most of the area consists of bare land and wetlands., while crops and built areas are concentrated in the Nile Wadi around the water body (i.e., Nile River) (Figure 6D).

3.2 Aeromagnetic results

Analyzing geophysical data is crucial to developing groundwater potential maps (GWPMs). Thus, the adopted, integrated, and holistic approach strongly contributes to groundwater potential mapping. Aeromagnetic data were initially used to outline basement rock configurations and identify subsurface fault patterns. This is crucial for comprehensively understanding the hydrogeological setting within the study area. The RTP map displays magnetic highs (H) and lows (L) with amplitudes ranging from −125 nT to 771 nT (Figure 7A). Three main magnetic minima characterize the study area's eastern, northwestern, and northeastern parts. L1 has a NW-SE strike, while L2 and L3 exhibit circular shapes. The magnetic maxima are situated in the study area's north-central, central, south-central, and southeastern portions. H1 trends in an N-S direction with a steep gradient, whereas H2 and H4 manifest as magnetic closures. H5 and H7 have NE-SW strikes, while H3 and H7 trend in a NW-SE direction. The high magnetic (H7) strike changes from NW-SE to nearly E-W direction.

3.2.1 Regional-residual separation

The magnetic signatures of any RTP anomaly map show superimposed anomalies originating from various sources. Long wavelengths characterize the regional anomalies and arise from deeply buried, sizable source bodies or structures. Regional anomalies are significant for investigating major tectonic features like oceanic ridges and subduction zones, while residual anomalies, characterized by short wavelengths, arise from shallow targets with geological significance (Lowrie, 2007). The primary focus of exploration geophysicists is to isolate residual anomalies, which serve as reliable indicators for identifying water reservoirs, hydrocarbon traps, mineral deposits, and other shallow geological targets of interest. A residual magnetic grid can be produced by eliminating the regional magnetic effect, thereby revealing the residual effects attributed to local structures (Griffin, 1949).

The regional magnetic map smoothes out high-frequency variations and highlights regional magnetic trends. (Figure 7B). The regional magnetic map highlights two magnetic lows (RL1 and RL2), nearly displaying circular shapes (Figure 7B). The map also shows high regional magnetic trends (RH1, RH2, and RH3), similar to those of the RTP map; however, the anomalies are simpler and smoother on the regional map than on the RTP map (Figure 7B). It also displays the area's main magnetic trends, including E-W, NW-SE, and NE-SW directions. The residual magnetic map shows the configuration of high and low magnetic anomalies. The map is highlighted with many linked anomaly closures (Figure 7C).

3.2.2 High-precision edge detection

In this study, six high-precision edge detection filters were selected to delineate and detect the edges of magnetic sources, including (ETilt, STDR, and impTDX (Figures 8A, B, respectively), ETHDR, THDR-STDR, and THDR-impTDX (Figures 9A–C, respectively). It is worth noting that in ETilt, STDR, and impTDX maps, edges of magnetic sources are highlighted by zero contour values, where they correspond to the maxima or peaks of the other three filters, as shown in Figure 8. According to the resulting maps, these filters are well-suited to delineate basement structures and offer noticeable advantages over other conventional techniques.

The ETilt (Figure 8A) and ETHDR (Figure 9A) filters provided sharp gradients over magnetic source boundaries, making them more effective for creating a detailed structural map of the study area. The STDR (Figure 8B) and THDR-STDR (Figure 9B) filters allow the edge detection of adjacent anomalies with superior accuracy and sharpness compared with other filters. These filters also successfully highlight anomalies' shapes (Nasuti et al., 2019). However, these filters exhibit noise sensitivity, resulting in superior results than other conventional filters due to the establishment of a trade-off between the image signal and noise (Othman and Ibraheem, 2024).

The impTDX (Figure 8C) and THDR_impTDX (Figure 9C) filters show high performance in detecting source boundaries, revealing sharper and more precise edges, and effectively detecting the boundaries of adjacent anomalies. These filters have various advantages, as they eliminate false edges and are less susceptible to noise than other popular filters, thus significantly eliminating the uncertainty in interpreting the results. The impTDX filter has values ranging from −1 to 1, resulting from the hyperbolic tangent function, with the maxima overlaying the entire source body. (Ibraheem et al., 2023). THDR_impTDX filter was applied as it produces maximum values along the edges of magnetic sources and sharply detects these boundaries. According to the results of the filters, the maps display the same magnetic trends in the NW-SE, NE-SW, N-S, and E-W directions.

The structural elements affecting groundwater accumulation are revealed through a detailed structural map derived from the integrated results (Figure 10). The structural map was created by selecting structural elements such as faults and contacts, which were verified through several techniques. The map clearly reveals four structural trends that dominate the area under study: NW-SE, NE-SW, N-S, and E-W, which have a significant effect on the structural framework. The delineated structures correspond to magnetic sources of different depths. The deduced structural map reveals the presence of several normal faults in the study area that demarcate a series of subsurface horsts (H) and grabens (G), which are intersected by lateral faults. Three main basins (A, B, and C) were identified, as shown in Figure 10. The structural map also indicates several changes in the course of the Nile River caused by these faults, most notably in the area between Gerga and Sohag cities and south Tahta city. The structural map also shows that the course of the Nile River is passing through the sedimentary basin (A) and is very close to the basin (B) (Figure 10).

3.2.3 Source parameter imaging (SPI)

Figure 11 shows the basement depth calculated using the SPI technique, along with polygons representing the main basins in the study area. The estimated depth is provided at the calculated location

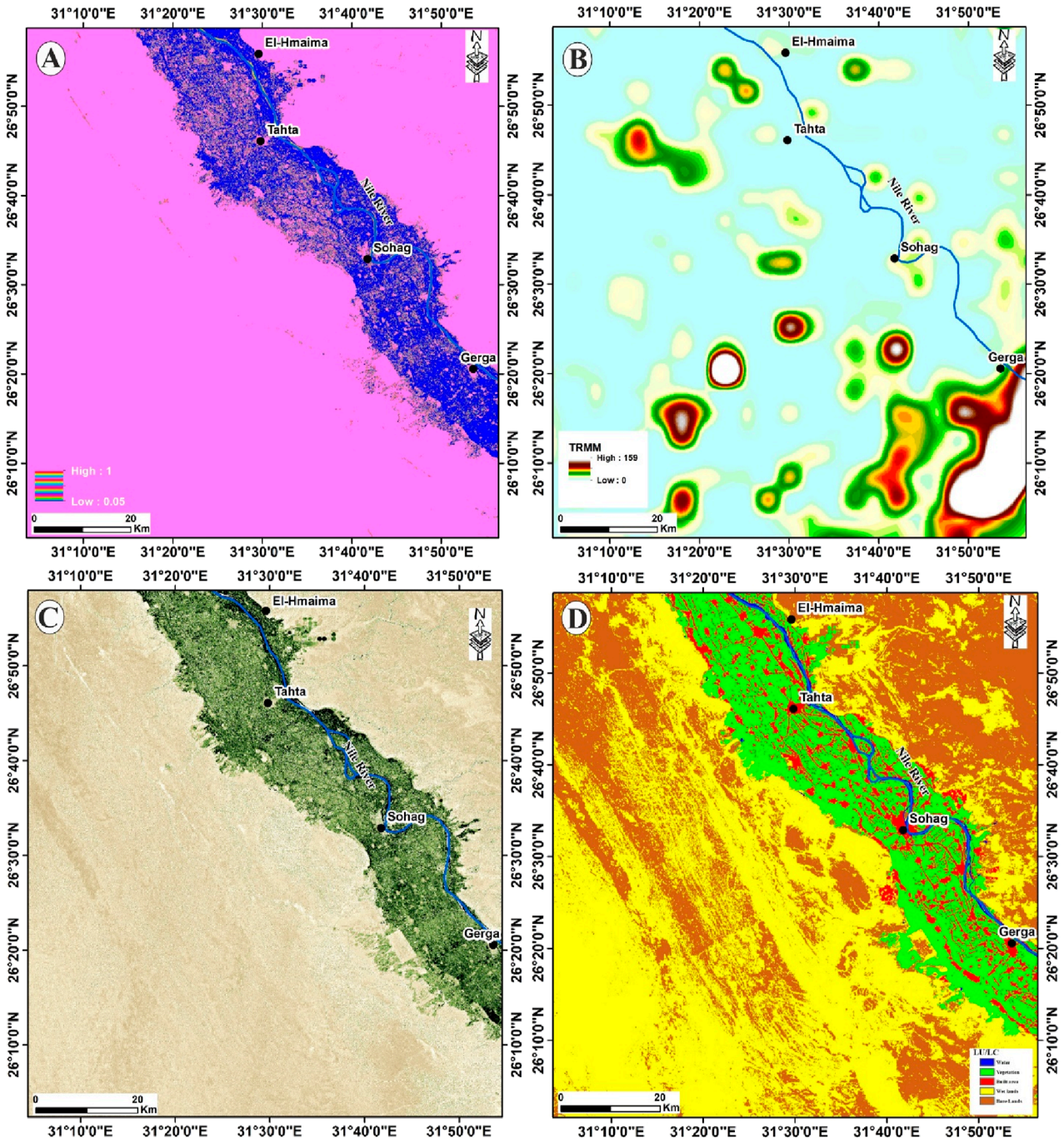

FIGURE 6
(A) Soile moisture. **(B)** Annual rainfall map in mm. **(C)** Sentinel 2 normalized difference vegetation index (NDVI) (B8-B4)/(B8 + B4). **(D)** Land use/land cover (LU/LC) map of the Sohag area.

and ranges from 870 to 4,020 m (Figure 11). Three main basins (A, B, and C) were identified as being the deepest areas (Figure 11). The greatest sediment thickness is in basins A and B. The basement depth reaches 3,760 m at basin A and about 4,020 m at basin B. Basin A is situated southeast of Sohag City, while basin B is located in the northwestern part of the study area. Basin C is situated in the western section and is of second priority, with a maximum depth to the basement of 2,800 m.

3.2.4 Modelling

Five (2D) magnetic models (P1-P1', P2-P2', P3-P3', P4-P4', and P5-P5') were constructed to get a geological description of the sedimentary cover and basement rocks using the GM-SYS modelling program (Geosoft, 2018). The basement complex in the study area is entirely subsurface, which hinders a better understanding of its nature. For the modelling process, the average magnetic susceptibility of basement rocks is assigned to

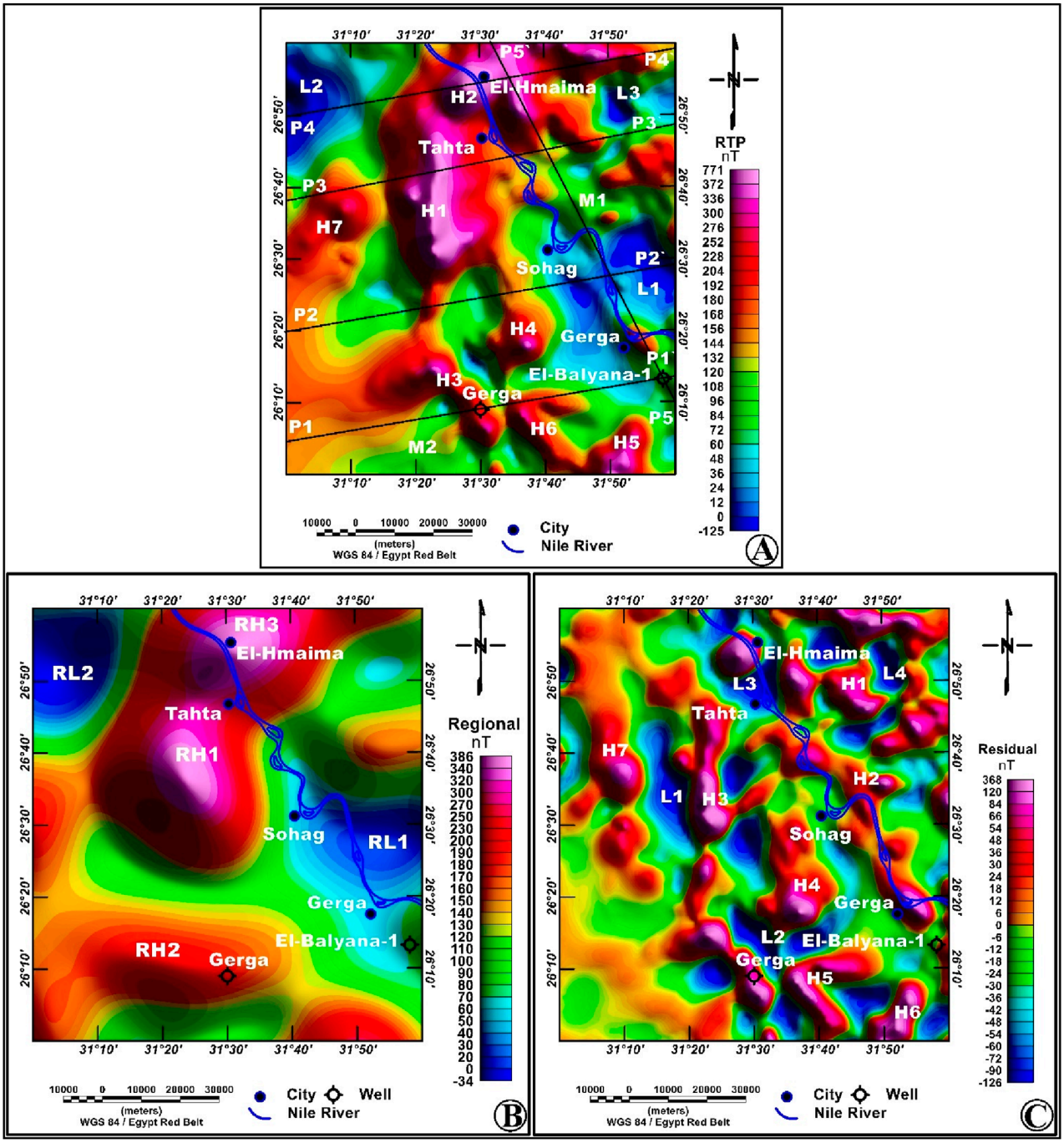

FIGURE 7
(A) The reduced-to-pole (RTP) map of the study area, with black lines, shows the location of selected 2D magnetic modelling profiles. **(B)** regional (low-pass) magnetic anomaly map. **(C)** residual (high-pass) magnetic anomaly map.

range between 0.025 and 0.033 cgs (Mohamed, 2021; Beshr et al., 2021). These values match the range of granitic rocks reported by Telford et al. (1990), as well as the susceptibility distribution of the Arabian-Nubian Shield basement rocks (0.022–0.034 cgs) determined by Hemant (2003). The sedimentary cover is generally non-magnetic and is assigned a magnetic susceptibility equal to zero. Therefore, these parameters were incorporated as constraints in the modeling process to minimize ambiguity and attempt to construct models as closely related as possible to the subsurface conditions.

Figure 12 and Table 3 show the results of the 2D magnetic models. The basement depth varies from 700 to 3,970 m, with a notable increase towards the Nile Valley. In the five models, the basement surface beneath the study area is disturbed by intrusions (e.g., The uplift observed at profile P3-P3', occurring at a depth range of 712 m and exhibiting a high magnetic susceptibility value

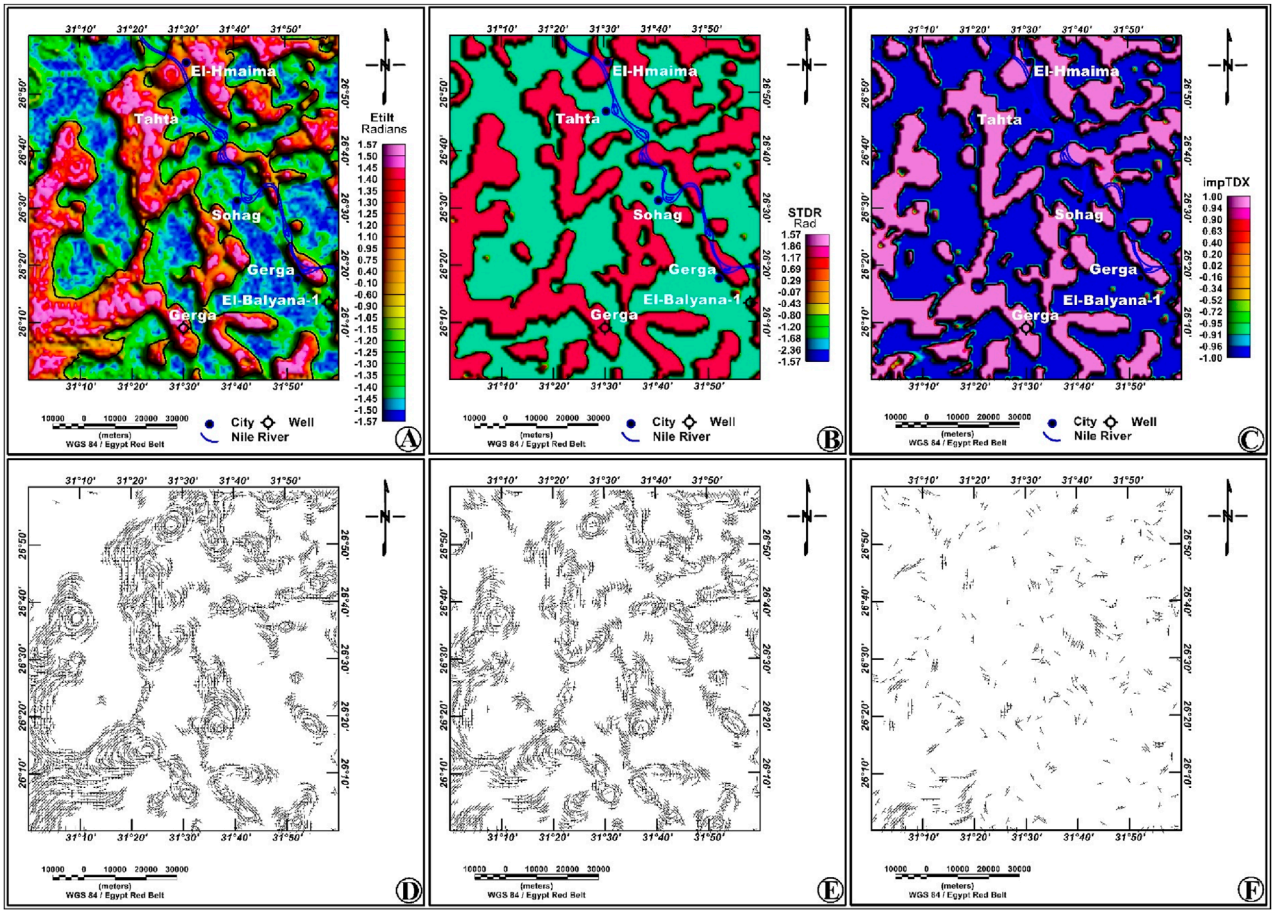

FIGURE 8
(A) ETilt. **(B)** STDR. **(C)** impTDX filters of the RTP aeromagnetic data show the edges of subsurface causative bodies. The source edge detection lineaments of the ETilt, STDR, and impTDX filters are shown in **(D, E, F)**, respectively.

of 0.033 cgs), indicating the occurrence of highly magnetized rocks. Normal faulting dissects the basement rocks, dividing them into tilted blocks that dip and progressively deepen as they move away from the uplifted zones (Figure 12). The depth reaches 3,970 m at the northwestern end of the profile (P4-P4'), corresponding to the estimated basin (B) in the northwestern portion of the study area (Figure 12). Also, the profiles (P1-P1'; P2-P2'; P5-P5') show a large thickness of the sedimentary cover, reaching up to 3,800 m at the eastern end of profile (P2-P2') related to the basin (A).

3.3 Data validation and integration in groundwater potentiality mapping

In this study, nine groundwater controlling parameters (soil moisture, rainfall, lithology, NDVI, drainage density, lineament density, slope, LU/LC, and RTP) were examined and classified based on study area characteristics, previous studies, and experts' opinions (Figure13). In ArcGIS, the various thematic layers were classed into five categories: (1) low, (2) moderate, (3) good, (4) very good, and (5) excellent in terms of their value concerning groundwater occurrence, and appropriate weights were assigned (Figure 13). In addition to the remote sensing thematic layers, the geophysical RTP layer supports groundwater potential mapping via serving as a beneficial indicator for recognizing main structural trends, estimating the sedimentary cover thickness, and providing information regarding the possible extension of the outlined subsurface basins.

The RTP map was reclassified into five categories, from 1 to 5 (Table 4; Figure 13). Category 5 (excellent) refers to the low magnetic values (less than 60 nano Tesla) shown in blue color in Figure 7A. The low magnetic values of category 5 are caused by thick sediments with low magnetic susceptibility. As sediment thickness and subsurface structures play a significant role in groundwater accumulations, low magnetic values were given higher weights, whereas high magnetic values (category 1) received lower weights. Similarly, categories 2, 3, and 4 were assigned moderate, high, and very high weights, respectively, based on their magnetic values and their values in groundwater occurrence.

AHP is utilized as a decision-making system for these characteristics based on their relative influence to correctly categorize the groundwater potentiality mapping of the investigated area by assigning a numerical value or weight to each pixel in the resulting thematic map that depicts the area's groundwater potential.

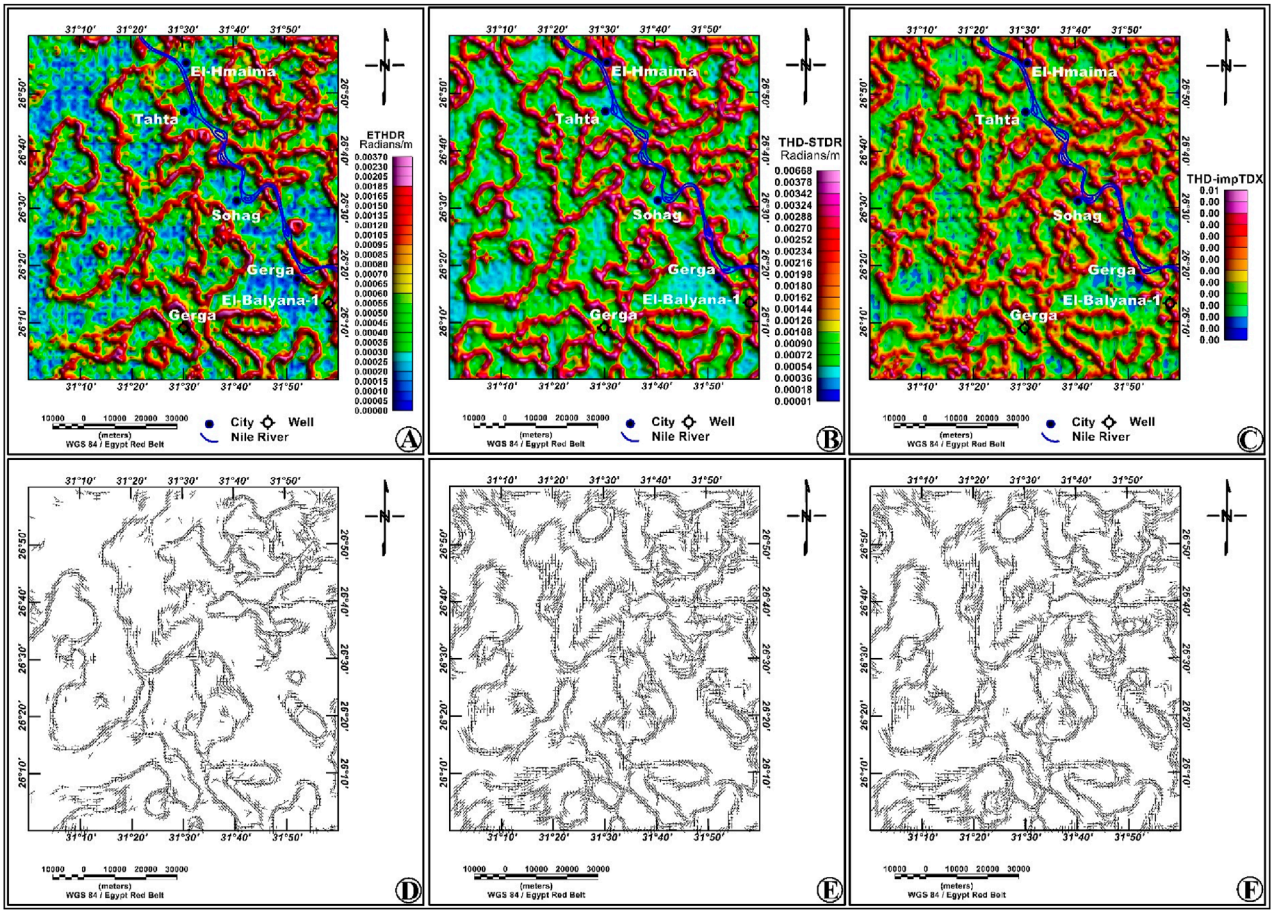

FIGURE 9
(A) ETHDR. **(B)** THDR-STDR. **(C)** THDR_impTDX filters of the RTP aeromagnetic data show the edges of subsurface causative bodies. The source edge detection lineaments of the ETHDR, THDR-STDR, and THDR_impTDX filters are shown in (**D, E, F**), respectively.

Based on thorough knowledge of the study area conditions and consultation with experts, we assigned weights to each criterion using a pairwise comparison method (Table 4). The scale proposed by Wind and Saaty, 1980, which is frequently utilized, simplifies comparisons by assigning a relative importance value that varies from 1 (signifying equal importance) to 9 (indicating extreme importance). This approach significantly facilitates the creation of a pairwise comparison matrix. Subsequently, the principal eigenvectors were normalized and calculated for each specific criterion (Table 5).

As a result of weight overlay analysis in ArcGIS, the groundwater potential mapping was created through the AHP model (Figure 14). The weight of each class inside each groundwater potential class is listed in Table 4. The soil moisture takes the highest weight at 26.8%, and the geophysical RTP layer takes the lowest weight at 4.4%. According to the groundwater potential mapping results, the excellent to very good potential classes show the location where water can be easily accessible (Figure 14). This map depicted that an area of about 3.225 km^2 is classified as very good, ~24.712 km^2 as good, ~32.566 km^2 as moderate, and 0.391 km^2 as the poor category of groundwater probability. The excellent potential groundwater zones are located in west Tahta City, on the western side of the Nile River, as sparse spots (red points in Figure 14). The very high potential groundwater zones occupy a relatively wide strip on the western side of the Nile Valley and a narrow belt on the eastern side. The high-potential groundwater zones are located in the northwestern and northeastern parts, as well as sparse spots on both sides of the Nile Valley. The area under the curve (AUC) can be used to assess the predictive performance of models, and a larger AUC indicates a better model (Echogdali et al., 2022; Ikirri et al., 2023). An approximate area under the curve (AUC) value of 86.2% was obtained on the validation using the area under the curve (AUC) method (Figure 15), which is very good accuracy.

4 Discussion

The automatic extraction of the surface structure lineaments reveals that the study area is mainly prevailed by the Red Sea-Gulf of Suez trend, with minor lineaments of both the Tethyan-Mediterranean and Nubian trends (Figure 3A). The majority of these lineaments are associated with the Eocene limestone plateaus, whereas the lineaments are absent in the valleys filled with the Quaternary alluvium (Figure 2B). Hence, it is believable that the

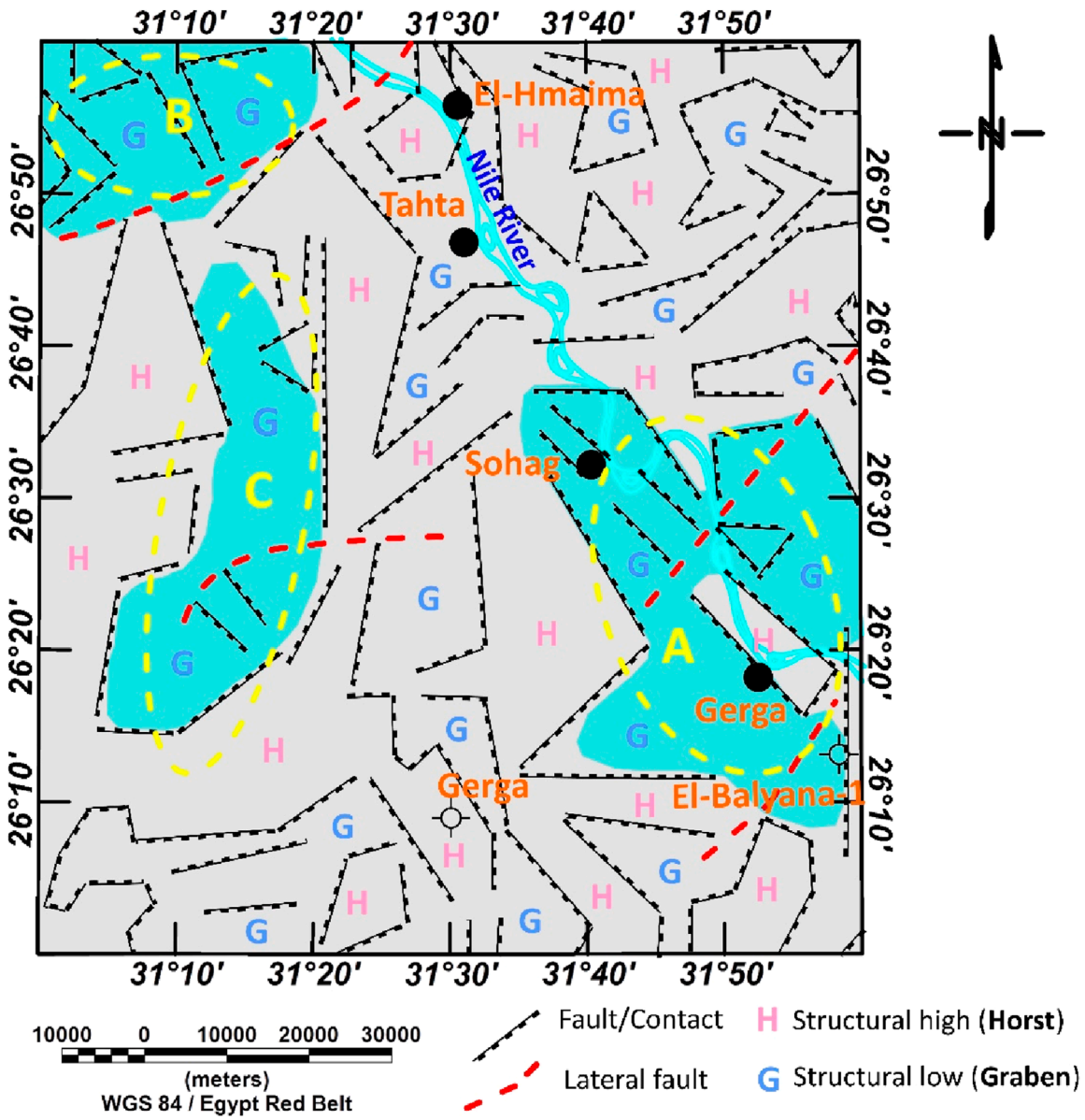

FIGURE 10
Interpreted basement structural element map of the study area derived from the magnetic data.

valley and its surrounding lineaments began to form subsequent to the Eocene age. They likely originated during the Oligocene and persisted into the Miocene, aligning with the Red Sea Hills uplift. The presence of gravel patches from the Katkut Formation on the Western Plateau, dated to the Oligocene by Issawi et al. (2009) and originating from the foundation rocks of the Eastern Desert, supports this evidence. Therefore, they were deposited before the Western Plateau separated, thus contributing to the formation of the valley. They were deposited before the completion of the limestone Plateau separation through the Qena System (Abotalib and Mohamed, 2013; Beshr et al., 2021). The valley cliffs are probably associated with subsurface faults, as they are lineament-controlled and straight for several kilometers (Beshr et al., 2021).

Figure 5A reveals that the DEM elevations reach 499 m on the plateau and decrease to 52 m along the alluvial floodplains. This variation in land surface serves to direct runoff from the higher plateau to the floodplain, enhancing its suitability for groundwater recharge. Besides, slope direction controls the groundwater flow direction and recharging, and consequently, groundwater potential (Figure 5B). The research area comprises gentle, moderate, and steep slopes that range from 0° to 68.11°, according to the slope map (Figure 5B). The study area is mainly flat except for steep slopes associated with wadi cliffs along the Nile River and the northern half (Figure 5B). The drainage network map reveals that the south Sohag and north Tahta regions are characterized by high drainage densities, as revealed by Figures 5D,E. Consequently, this leads to

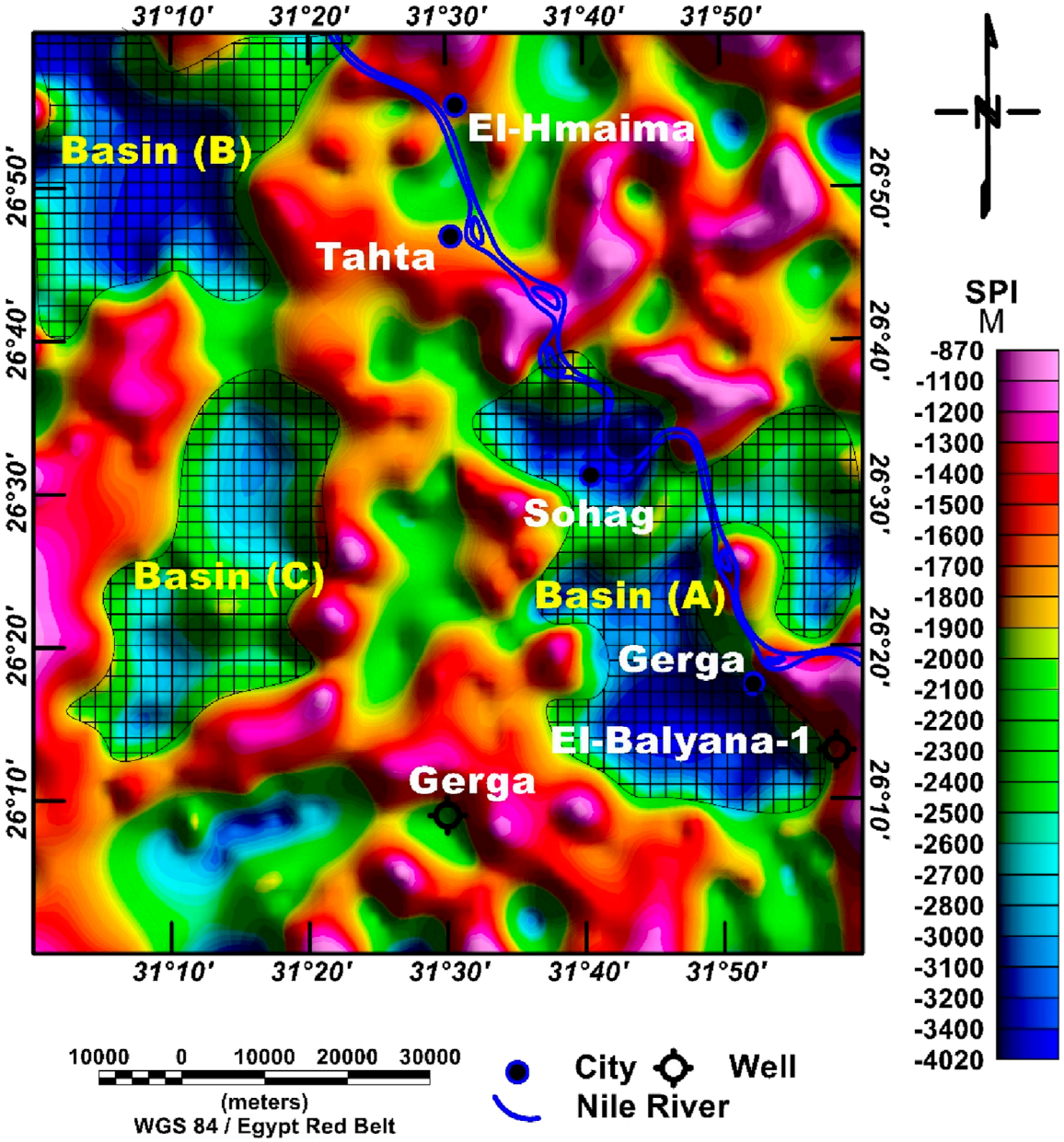

FIGURE 11
A magnetic source depth map, based on the SPI technique, shows the main subsurface basins.

increased runoff and reduced groundwater potentiality compared to other parts of the study area.

The estimated NDVI map reflects dense vegetation around the Nile River path, which decreases as moving away from the river (Figure 6C). The LU/LC map of the Sohag region revealed that farmed lands and building areas are concentrated around the water body (i.e., Nile River) in the Nile Wadi district, whereas most of the region comprises of wetlands and bare (Figure 6D).

Regarding the magnetic data, the high magnetic anomalies (H1-H7) shown by the RTP map (Figure 7A) might be related to uplifted basement blocks or the existence of igneous intrusions of high magnetic values. These high magnetic anomalies are further confirmed by our 2D magnetic models, which reveal several igneous intrusions (Figure 12). Conversely, low magnetic anomalies (L1 and L2) could be linked to deep basement rocks beneath a thick low-magnetization sedimentary cover. These low magnetic anomalies are further confirmed and emphasized by the regional magnetic map (Figure 7B). The regional low magnetic (RL1) is related to the main basin of the Sohag area, while the other one (RL2) is associated with the western extension of the Wadi El Assiuti Basin, as stated by a previous geophysical study conducted by Mohamed and Abu El-Ella (2023). The residual magnetic map shows and enhances the configuration of several high and low magnetic anomalies (Figure 7C). The map is highlighted with many

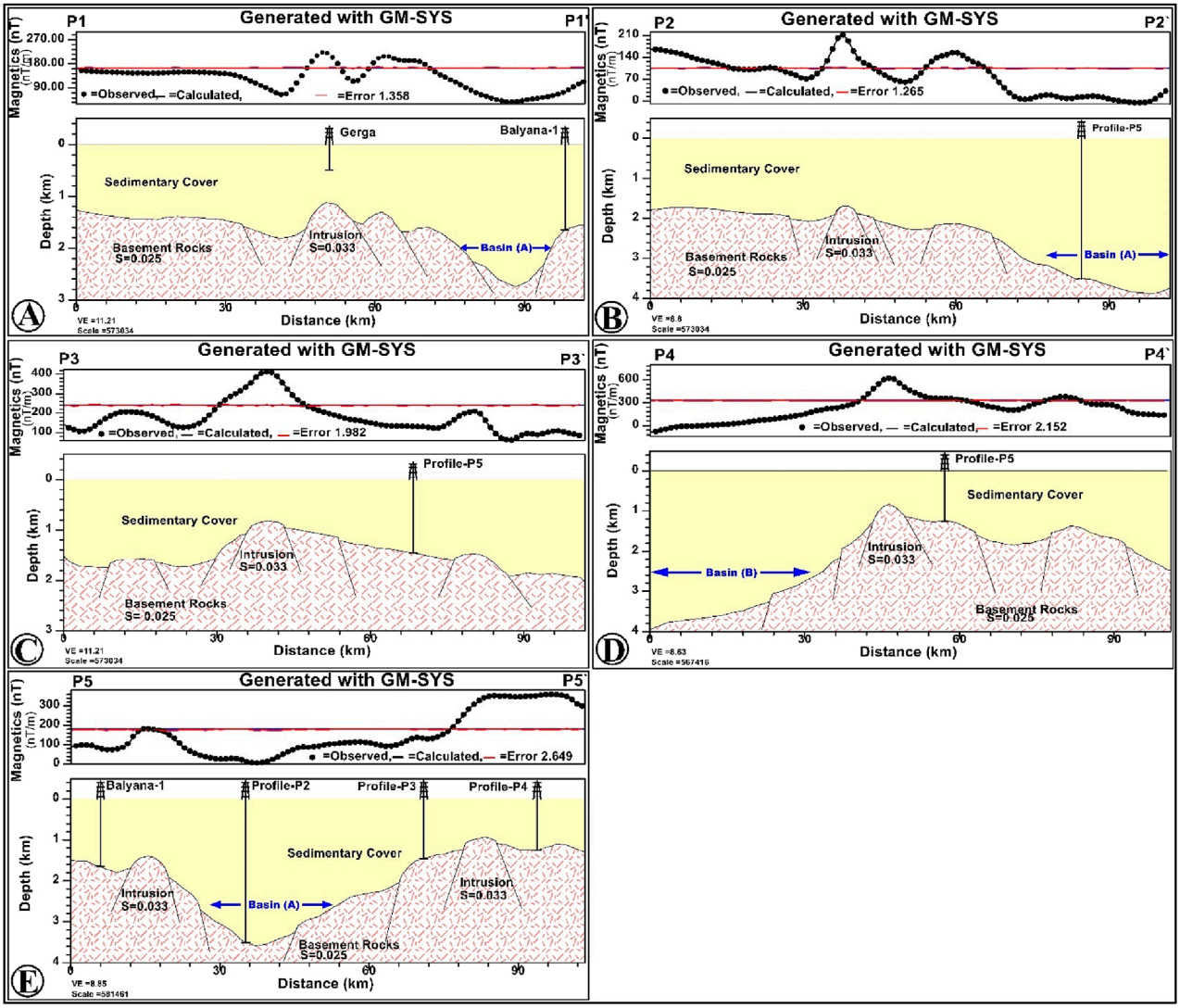

FIGURE 12
The 2D magnetic susceptibility models for the profiles **(A)** P1-P1′, **(B)** P2-P2′, **(C)** P3-P3′, **(D)** P4-P4′ and **(E)** P5-P5`.

TABLE 3 Description of 2D magnetic models.

Magnetic profile	Direction	Length (Km)	Magnetic reading (nT)	Basement depth (m)
P1-P1′	NE-SW	101.48	38–223	1,122–2,750
P2-P2′	NE-SW	101.22	−5–210	1,687–3,800
P3-P3′	NE-SW	101.40	64–412	712–2059
P4-P4′	NE-SW	100.57	−86–627	825–3,970
P5-P5′	NW-SE	102.95	5–361	926–3,591

linked anomaly closures, suggesting the presence of supra-basement positives and structures varying in shape, depth, and trend. The anomalies predominantly extend in the NW, NE, N-S, and E-W directions.

The high-precision edge detection techniques (Figures 8, 9) can fruitfully highlight the shapes of the magnetic anomaly sources (Nasuti et al., 2019), resulting in superior results than other conventional filters (Othman and Ibraheem, 2024). These

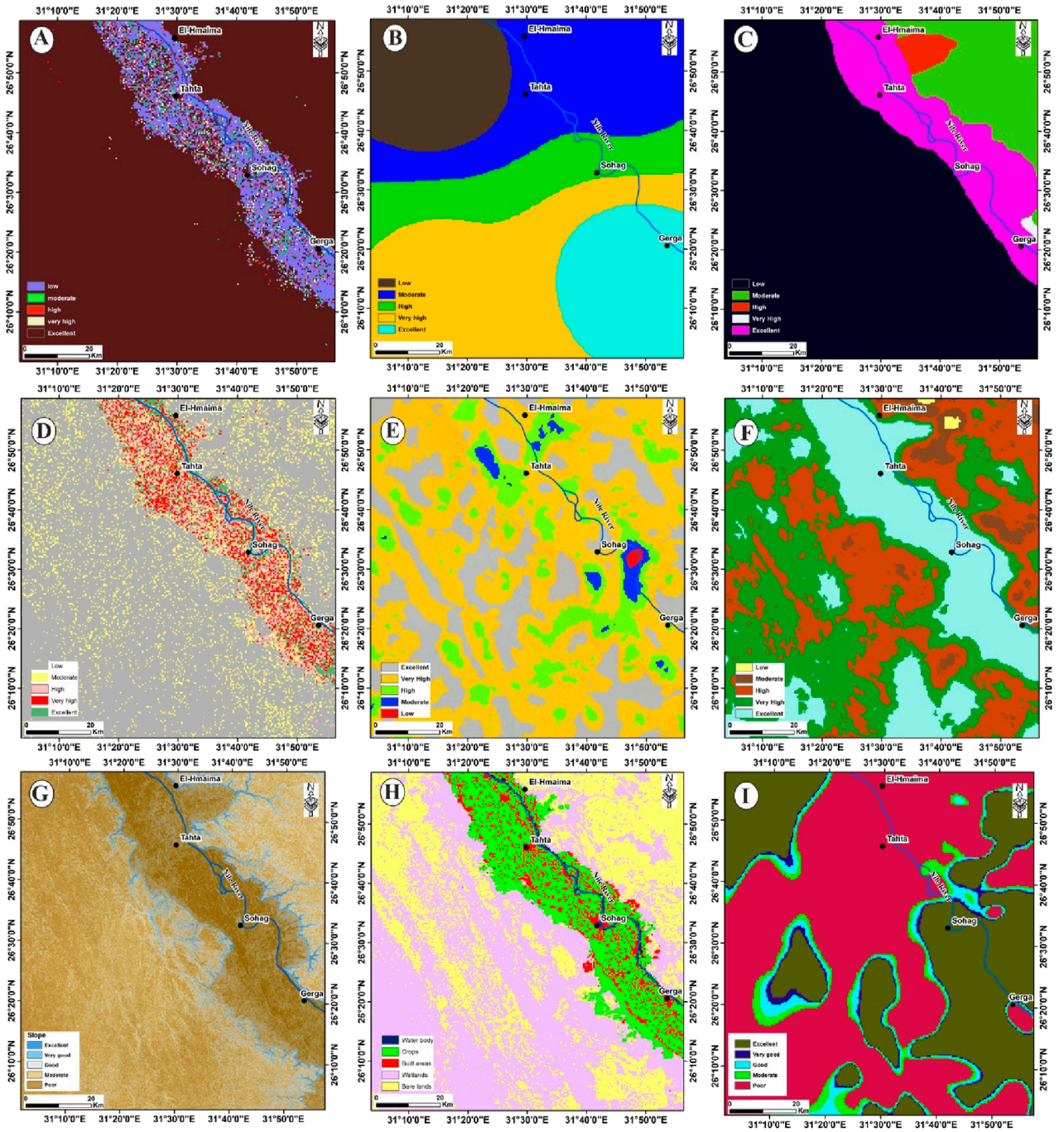

FIGURE 13
Reclassified maps of **(A)** Soil moisture, **(B)** Rainfall, **(C)** Lithology, **(D)** NDVI, **(E)** Drainage density, **(F)** Lineament density, **(G)** Slope, and **(H)** LU/LC, **(I)** RTP of the study area.

techniques delineate the basement structure better than other conventional techniques due to their advantages (Ibraheem et al., 2023; Pham et al., 2023). As a result, these filters can give clearer and more detailed views of the structural setting in the study area (Figure 10). Although ETILT and ETHDR filters enhance magnetic data interpretation, their limitations must be acknowledged. Specifically, they generated false edges in the southwestern part of the study area (Figure 8A). Hence, these filters should be integrated with more advanced techniques such as STDR and impTDX filters and supported by geological knowledge to enhance results accuracy (Ibraheem et al., 2023). Although the STDR and impTDX filters are highly effective in mapping the edges of source bodies, they can still be affected by noise (Figures 8, 9). The structural setting map (Figure 10) clearly reveals four structural trends that dominate the area under study: NW-SE, NE-SW, N-S, and E-W, which is supported

10.3389/feart.2024.1456055

TABLE 4 Rank, score, and weight assigned for the nine parameters.

Rank	Thematic layer	Class	Score	Weight
1	SM	0.02–0.05	1	0.268
		0.05–0.07	2	
		0.07–0.10	3	
		0.10–0.15	4	
		0.15–0.31	5	
2	RF	0–0.6	1	0.189
		0.6–21	2	
		21–45	3	
		45–92	4	
		92–159	5	
3	L	Eocene thick marine limestone	1	0.133
		Pliocene marine bed	2	
		Pre-Nile sediments	3	
		Undivided Quaternary deposits	4	
		Nile deposits	5	
4	NDVI	−0.5–0.2	1	0.099
		0.2–0.4	2	
		0.4–0.6	3	
		0.6–0.8	4	
		0.8–1.0	5	
5	DD	74.40–142.65	5	0.074
		53.70–74.40	4	
		38.59–53.70	3	
		38.59–38.59	2	
		0–23.49	1	
6	LD	0–0.11	1	0.072
		0.12–0.26	2	
		0.27–0.39	3	
		0.40–0.52	4	
		0.53–0.98	5	

(Continued on the following page)

TABLE 4 (*Continued*) Rank, score, and weight assigned for the nine parameters.

Rank	Thematic layer	Class	Score	Weight
7	S (°)	27–68	5	0.068
		15–26	4	
		7.8–14	3	
		3.8–7.7	2	
		0–3.7	1	
8	LU/LC	Bare lands	1	0.053
		Wet lands	2	
		Built areas	3	
		Crops	4	
		Water body	5	
9	RTP	<60 nano Tesla	5	0.044
		60–120 nano Tesla	4	
		120–180 nano Tesla	3	
		180–240 nano Tesla	2	
		>240 nano Tesla	1	

Notes: SM, soil moisture; RF, rainfall; L, lithology; NDVI, normalized difference vegetation index; DD, drainage density; LD, lineament density; S, slope; LU/LC, landuse/landcover.

TABLE 5 Pairwise comparison matrix for the nine parameters.

Thematic layer	SM	RF	L	NDVI	DD	LD	S (°)	LU/LC	RTP
SM	1	7	5	7	3	1	5	3	3
RF	1/7	1	3	7	5	5	3	5	1
L	1/5	1/3	1	5	3	1	3	5	5
NDVI	1/7	1/7	1/5	1	5	3	5	1	1
DD	1/3	1/5	1/3	1/5	1	1	3	1	5
LD	1	1/5	1	1/3	1	1	1	1	1
S (°)	1/5	1/3	1/3	1/5	1/3	1	1	5	3
LU/LC	1/3	1/5	1/5	1	1	1	1/5	1	3
RTP	1/3	1	1/5	1	1/5	1	1/3	1/3	1

by the residual magnetic map (Figure 7C). These structural trends have a significant effect on the structural framework. The observed fault trends are in agreement with the geological trends reported previously by Said (1962) and Ibraheem et al. (2019). The structural setting map also illustrates the Nile River flowing through the sedimentary basins (A) and near basin (B), suggesting that surface water continues to recharge these basins (Figure 10). These results are supported by several studies, including (Said 1981; Said 1990; Said 1994; Youssef 2003; Mohamed 2021; Woodward et al., 2022), and others, who suggested that the Nile grabens originated from Red Sea opening-related tectonic movements.

The calculated depth using the source parameter imaging varies between 870 and 4,020 m (Figure 11). This depth range

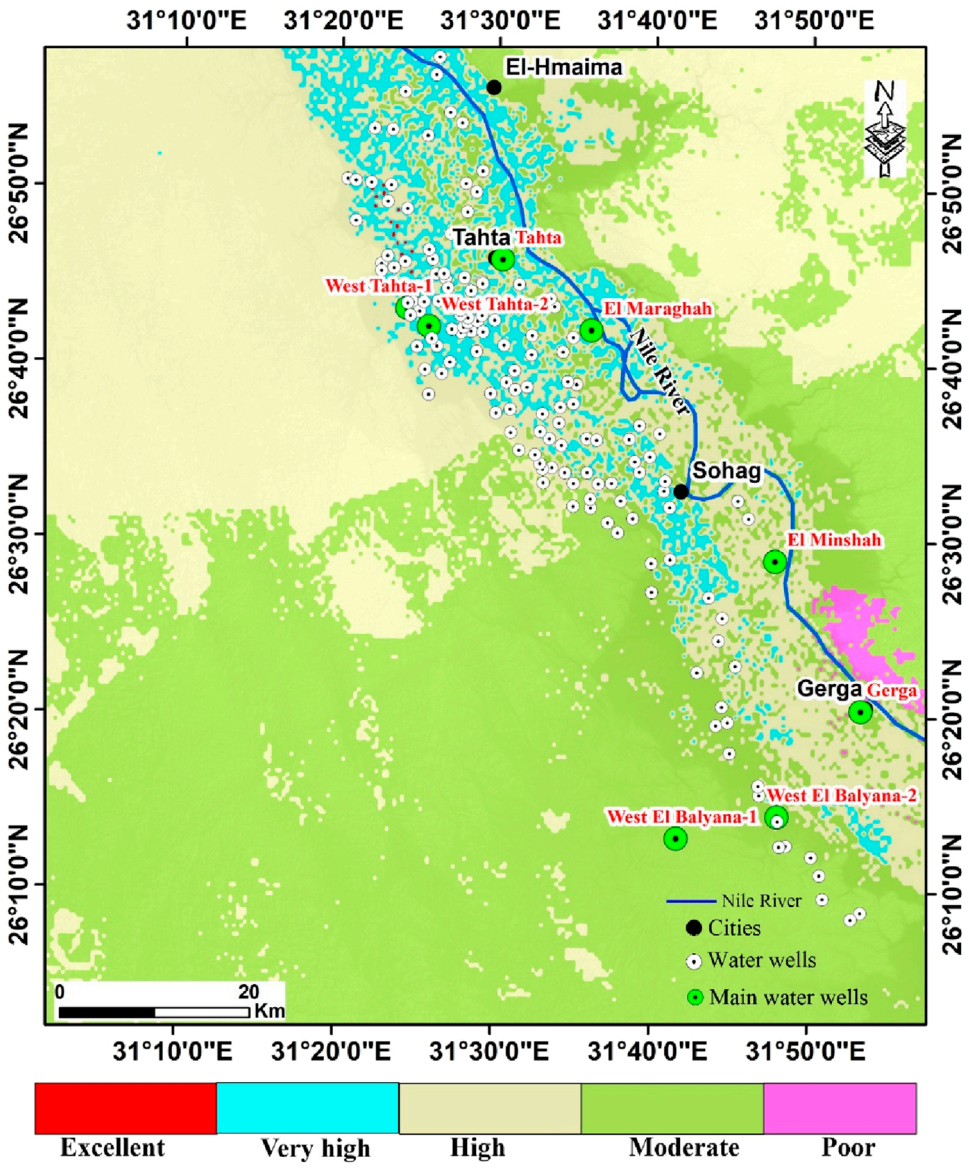

FIGURE 14
A groundwater potential map was constructed by integrating nine remote sensing and geophysical parameters.

agrees to an acceptable extent with the results obtained from the study of Ghazala et al. (2018a), who concluded that the basement depth varies between 400 and 4,000 m. Also, the source parameter map outlines three sedimentary basins (A, B, and C) with the greatest sedimentary thickness in the A and B basins. Basin A is located southeast of Sohag and has about 3,760 m sedimentary section, whereas basin B occupies the northwestern portion of the study area and has about 4,020 m sedimentary section. These two basins represent the most promising zones for groundwater accumulations. Basin C is located on the western side, with about 2,800 m depth to the basement, and represents a secondary priority for water accumulation.

The 2D magnetic susceptibility models reveal a depth to the basement varying between 700 and 3,970 m, with a distinguished increase towards the Nile Valley region (Figure 12). The maximum depth value of about 3,970 m is recorded at the northwestern end of the P4-P4' profile, corresponding to basin (B). Additionally, the other three magnetic profiles indicate a substantial sedimentary cover, reaching up to 3,800 m at the eastern end of the P2-P2' profile beneath basin (A). The basement rocks beneath the study area are interpreted to be of granitic composition. This conclusion is supported by the subsurface record of the basement rock available at the El-Balyana borehole at a depth of 1,640 m in the southeastern region (Nabih, 2005). Also, Several earlier geological and geophysical studies in nearby areas concluded that basement rocks are of granitic composition (e.g., Said, 1962; Ghazala et al., 2018a; 2018b; Mohamed, 2021; Beshr et al., 2021).

Additionally, granite exposures can be found further south around Aswan along the Nile (El-Gammal et al., 2013). The models reveal many high magnetic susceptibility igneous intrusions,

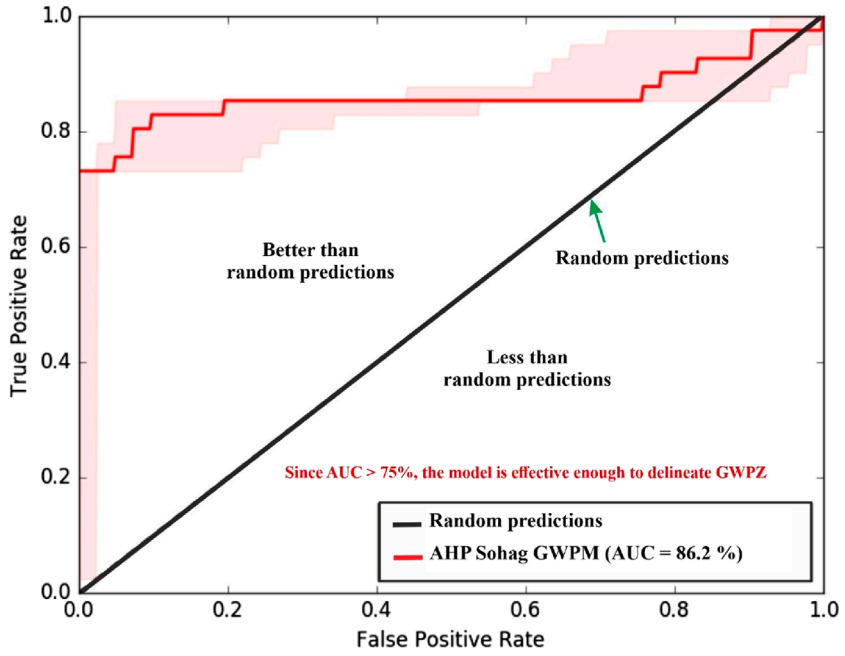

FIGURE 15
AUC curve of the GWPM in the Sohag area.

disrupting the study area's basement rocks (Figure 12). In line with Clark and Emerson (1991) and Hunt et al. (1995), these results suggest that these intrusive bodies are likely granodiorite rocks. As the basement depth increases, it suggests a significant rise in groundwater potentiality, likely attributable to thicker groundwater-bearing layers. The Oligo-Miocene uplift of Red Sea Rift shoulders affected the surrounding crust with tensile stress to the west. This event led to NW-SE fractures and cracks, which supported Nile Valley development and created secondary porosity, which improved the study area's hydraulic conductivity (Abdelkareem and El-Baz, 2015).

The groundwater potential map divided the study area into five classes ranging from excellent to poor potential (Figure 14). The most promising groundwater potential zones are located on the western side of the Nile River. According to RIGW (2023), spatial investigation of production water wells in the Sohag area confirms our findings (Figure 14; Table 1). The main eight water well production well sites are primarily located on the western side of the Nile River, which has more groundwater potential than the eastern side. These production water wells revealed reasonable allocation where these wells are located in the excellent, very high, and high potential groundwater zones (Figure 14). Additionally, there are one hundred forty-eight wells distributed along the Nile River, particularly in the western part (Figure 14) (Ismail and El-Rawy, 2018). Excellent potential groundwater zones that occur west of Tahta City, as shown in Figure 14. This conclusion matches well with the results of Esam et al. (2012), who conducted a groundwater quality study using hydrochemistry analysis in West Thata City. Besides, zones with very high groundwater potentiality occur in a relatively wide belt on the western Nile Valley and a narrow strip on the eastern side of the Nile Valey. In addition, zones with high groundwater potential occupy the northeastern and northwestern parts and scattered spots on both sides of the Nile Valley. These results are similar to other studies around the Nile River and the Sinai Peninsula (Abuzied and Alrefaee, 2017; Gaber et al., 2020; Shebl et al., 2022).

The potential groundwater map had several notable limitations, including 1) obtaining detailed geospatial data for the study area proved challenging, which likely impacted the accuracy of the data; 2) errors in the classification of maps and images, potentially due to their low resolution, may have further decreased the reliability of the information (Ikirri et al., 2023); 3) utilizing higher-resolution satellite imagery could enhance data extraction efficiency and improve the quality of the resulting factor maps (Echogdali et al., 2022); 4) the weightings assigned to the various factors were based on expert opinions, which inherently involve subjective judgments that can affect their assignment. However, some studies were able to generate a GWP map without incorporating these factors (Mukherjee Singh 2020; Al–Djazouli et al., 2021; Dar et al., 2021; Shebl et al., 2022; Ally et al., 2024).

In this study, we validate the potentiality map based on the distribution of existing water wells around the Nile River (Figure 14). The validated GWPM based on the AUC techniques indicates an 86.2% value, signifying that the accuracy of the model was very good in delineating groundwater potential zones in the study area (Figure 15). These results are supported by similar studies (Tehrany et al., 2014; Hong et al., 2018; Ally et al., 2024). The findings highlight the utility of integrating remote sensing-based GIS and aeromagnetic data through the AHP technique. This synergistic approach provides access to advanced analytical capabilities for studying and managing groundwater resources (Das et al., 2017; Mukherjee et al., 2020;

AlDjazouli et al., 2021; Dar et al., 2021; Shebl et al., 2022; Ikirri et al., 2023; Ally et al., 2024).

5 Conclusion

The present study demonstrated the effectiveness of the AHP method using remote sensing and aeromagnetic data in identifying groundwater potential zones in the Sohag area, Upper Egypt. Key surface parameters influencing groundwater infiltration and storage were identified, including soil moisture, rainfall, lithology, NDVI, drainage density, lineament density, slope, land use/land cover. Besides, the RTP aeromagnetic map was employed to delineate the subsurface structure and sediment thickness that control groundwater flow and accumulation. Three basins were outlined as the most promising zones for groundwater accumulation. The study area has been categorized into five distinct zones ranging from excellent to poor, according to the groundwater potential map. The excellent and very high groundwater potential zones are primarily clustered in the Nile Wadi deposits within the Nile Valley strip. These findings are corroborated by the spatial alignment of eight production water wells in the study area. The results can assist in watershed management by indicating optimal locations for well drilling and areas to avoid. This strategic approach can lead to more efficient and cost-effective groundwater exploration and development. The methodological framework and findings of this study also have the potential for broader application in regions with similar climatological conditions, geomorphological characteristics, and water scarcity challenges. Additionally, we recommend conducting detailed hydrogeological studies in the high groundwater potential zones located in the northeastern and northwestern regions, as these areas present promising targets for future development and industrial national projects.

Data availability statement

The original contributions presented in the study are included in the article/supplementary material, further inquiries can be directed to the corresponding authors.

Author contributions

HE-B: Conceptualization, Data curation, Resources, Supervision, Validation, Writing–review and editing. AA: Investigation, Supervision, Writing–review and editing. UM: Investigation, Supervision, Writing–review and editing. TA-A: Funding acquisition, Resources, Validation, Writing–review and editing. HA: Supervision, Validation, Writing–review and editing. SA: Methodology, Software, Validation, Writing–original draft. MN: Conceptualization, Data curation, Formal Analysis, Investigation, Methodology, Software, Validation, Visualization, Writing–original draft, Writing–review and editing.

Funding

The author(s) declare that financial support was received for the research, authorship, and/or publication of this article. This research received funding from the Open Access publishing fund from UiT, the Arctic University of Norway. We would like to express our sincere gratitude to UiT, which has made the publication of this work possible.

Acknowledgments

The authors acknowledge the UiT, the Arctic University of Norway, for open access funding.

Conflict of interest

The authors declare that the research was conducted in the absence of any commercial or financial relationships that could be construed as a potential conflict of interest.

Publisher's note

All claims expressed in this article are solely those of the authors and do not necessarily represent those of their affiliated organizations, or those of the publisher, the editors and the reviewers. Any product that may be evaluated in this article, or claim that may be made by its manufacturer, is not guaranteed or endorsed by the publisher.

References

Abdelkareem, M., and El-Baz, F. (2015). Analyses of optical images and radar data reveal structural features and predict groundwater accumulations in the central Eastern Desert of Egypt. *Arab. J. Geosci.* 8, 2653–2666. doi:10.1007/s12517-014-1434-7

Abd El Aal, A. K., Nabawy, B. S., Aqeel, A., and Abidi, A. (2020). Geohazards assessment of the karstified limestone cliffs for safe urban constructions, Sohag, West Nile Valley. *J. Afri. Ear. Sci.* 161, 103671. doi:10.1016/j.jafrearsci.2019.103671

Abdel-Moneim, A. (1988). *Hydrogeology of the nile basin in Sohag province*. Egypt: Geology Department, Faculty of Science, Assiut University.

Abo Khashaba, S. M., El-Shibiny, N. H., Hassan, S. M., Takazawa, E., and Khedr, M. Z. (2023). Application of remote sensing data integration in detecting mineralized granitic zones: a case study of the Gabal Al-Ijlah Al-Hamra, Central Eastern Desert, Egypt. *J. Asian Earth Sci.* 200, 104855. doi:10.1016/j.jafrearsci.2023.104855

Abotalib, A. Z., and Mohamed, R. S. (2013). Surface evidences supporting a probable new concept for the river systems evolution in Egypt: a remote sensing overview. *Environ. Earth Sci.* 69, 1621–1635. doi:10.1007/s12665-012-1998-z

Abu-ElMagd, S. A. (2008). Evaluation of the aquifer potentiality and land suitability for development in the desert area surrounding Sohag Governorate, Egypt; using geographic information systems. *M. Sc. Thesis, Geol. Dept., Fac. Sci.*

Abuzied, S. M., and Alrefaee, H. A. (2017). Mapping of groundwater prospective zones integrating remote sensing, geographic information systems

and geophysical techniques in El-Qaà Plain area, Egypt. *Hydrogeol. J.* 25, 2067–2088. doi:10.1007/s10040-017-1603-3

Aero Service Division of the Egyptian Nile Valley Petroleum Company (1993). *The reduced-to-pole magnetic intensity map, upper Egypt of scale 1:250,000. Aero service division the Egyptian Nile Valley Petroleum Company*. Cairo, Egypt.

Al-Badani, M. A., and Al-Wathaf, Y. M. (2018). Using the aeromagnetic data for mapping the basement depth and contact locations, at southern part of Tihamah region, western Yemen. *Egypt. J. Pet.* 27, 485–495. doi:10.1016/j.ejpe.2017.07.015

Aldeep, M., Araffa, S. A. S., Mansour, S. A., Taha, A. I., Mohamed, A., and Othman, A. (2021). Geophysics and remote sensing applications for groundwater exploration in fractured basement: a case study from Abha area, Saudi Arabia. *J. Afr. Earth Sci.* 184, 104368. doi:10.1016/j.jafrearsci.2021.104368

Al-Djazouli, M. O., Elmorabiti, K., Rahimi, A., Amellah, O., and Fadil, O. A. M. (2021). Delineating of groundwater potential zones based on remote sensing, GIS and analytical hierarchical process: a case of Waddai, eastern Chad. *Geo. J.* 86, 1881–1894. doi:10.1007/s10708-020-10160-0

Ally, A. M., Yan, J., Bennett, G., Lyimo, N. N., and Mayunga, S. D. (2024). Assessment of groundwater potential zones using remote sensing and GIS-based fuzzy analytical hierarchy process (F-AHP) in Mpwapwa District, Dodoma, Tanzania. *Geosystems Geoenvironment* 3 (1), 100232. doi:10.1016/j.geogeo.2023.100232

Araffa, S., Alrefaee, H., and Nagy, M. (2020). Potential of groundwater occurrence using geoelectrical and magnetic data: a case study from south Wadi Hagul area, the northern part of the Eastern Desert. Egypt. *J. Afr. Earth Sci.* 172, 103970. doi:10.1016/j.jafrearsci.2020.103970

Araffa, S. A. S., El-bohoty, M., Heleika, M. A., Mmekkawi, M., Ismail, E., Khalil, A., et al. (2018). Implementation of magnetic and gravity methods to delineate the subsurface structural features of the basement in central Sinai area, Egypt. *NRIAG J. Astron. Geophys.* 7, 162–174. doi:10.1016/j.nrjag.2017.12.002

Araffa, S. A. S., Sabet, H. S., and Mahmoud, M. H. (2023). Delineation of Nubian sandstone aquifer using geophysical data around Nuweiba area, Sinai, Egypt. *Appl. Water Sci.* 13, 187. doi:10.1007/s13201-023-01978-3

Arisoy, M., and Dikmen, Ü. (2013). Edge detection of magnetic sources using enhanced total horizontal derivative of the Tilt angle. *Bull. Earth Sci. Appl. Res. Cent. Hacet. Univ.* 34, 73–82.

Arulbalaji, P., Padmalal, D., and Sreelash, K. (2019). GIS and AHP techniques based delineation of groundwater potential zones: a case study from southern western ghats, India. *Sci. Rep.* 9, 2082. doi:10.1038/s41598-019-38567-x

Arunbose, S., Srinivas, Y., Rajkumar, S., Nair, N. C., and Kaliraj, S. (2021). Remote sensing, GIS and AHP techniques based investigation of groundwater potential zones in the Karumeniyar river basin, Tamil Nadu, southern India. *Groundw. Sustain. Dev.* 14, 100586. doi:10.1016/j.gsd.2021.100586

Ashmawy, M. H., Abd El-Wahed, M. A., Kamh, S. Z., and Shebl, A. (2018). Comparative study of the drainage basin morphometry extracted from topographic maps and SRTM DEMs: an example from Ghadir watershed, Eastern Desert, Egypt. *Sci. J. Basic Appl. Sci.* 39, 52–64.

Attia, F. A. (1974). *Parameter and characteristics of the groundwater reservoir in Upper Egypt*. Egypt: Cairo Univ.

Baranov, V. (1957). Anew method for interpretation of aeromagnetic maps: pseudo-gravimetric anomalies. *Geophysics* 22, 359–382. doi:10.1190/1.1438369

Baranov, V., and Naudy, H. (1964). Numerical calculation of the formula of reduction to the magnetic pole. *Geophys. J.* 29, 67–79. doi:10.1190/1.1439334

Beshr, A. M., Kamel Mohamed, A., ElGalladi, A., Gaber, A., and El-Baz, F. (2021). Structural characteristics of the Qena bend of the Egyptian Nile River, using remote-sensing and geophysics. *J. Remote Sens. Space Sci.* 24, 999–1011. doi:10.1016/j.ejrs.2021.11.005

Blakely, R. J. (1996). *Potential theory in gravity and magnetic applications*. 1st ed. Cambridge, UK: Cambridge University Press, 441p.

Clark, D. A., and Emerson, D. W. (1991). Notes on rock magnetization characteristics in applied geophysical studies. *Explor. Geophys.* 22, 547–555. doi:10.1071/EG991547

Conoco (1987). *Geological map of Egypt, scale 1:500,000, sheet NG36NW asyut, Egypt*. Cairo, Egypt: The Egyptian General Petroleum Corporation.

Dar, T., Rai, N., and Bhat, A. (2021). Delineation of potential groundwater recharge zones using analytical hierarchy process (AHP). *Geol. Ecol.Landsc.* 5, 292–307. doi:10.1080/24749508.2020.1726562

Das, S., Gupta, A., and Ghosh, S. (2017). Exploring groundwater potential zones using MIF technique in semi-arid region: a case study of Hingoli district, Maharashtra technique in semi-arid region: a case study of Hingoli district, Maharashtra. *Spat. Inf. Res.* 25, 749–756. doi:10.1007/s41324-017-0144-0

Diab, M. S. (1972). *Hydrogeological and hydrochemical studies of theNubian sandstone water-bearing complex in some localities inUnited Arab Republic*. Egypt: Assiut University. PhD Thesis.

Dobrin, M. B., and Savit, C. H. (1988). *Introduction to geophysical prospecting*. 4th ed. New York, NY, USA: McGraw-Hill.

Echogdali, F. Z., Boutaleb, S., Bendarma, A., Saidi, M. E., Aadraoui, M., Abioui, M., et al. (2022). Application of analytical hierarchy process and geophysical method for groundwater potential mapping in the Tata basin, Morocco. *Water* 14, 2393. doi:10.3390/w14152393

EGSMA. (1981). Geologic map of Egypt. Ministry of industry and mineral resources. The Egyptian geological survey and mining authority.

Elbeih, S. F., Madani, A. A., and Hagage, M. (2021). Groundwater deterioration in Akhmim District, Upper Egypt: a remote sensing and GIS investigation approach. *Egypt. J. Remote Sens. Space Sci.* 24 (3), 919–932. doi:10.1016/j.ejrs.2021.10.002

El-Gammal, E. A., Salem, S. M., and Greiling, R. O. (2013). Geology, morphotectonics and geophysical interpretation of wadi garara graben, east aswan Egypt, using landsat images. *Aust. J. Basic Appl. Sci.* 7, 263–277.

El-Sabri, M. S. (2011). Assessment of water logging problem in the area between El monshah and El Balyana, west Nile Valley, south Sohag, Egypt. *J. Environ. Sci.* 40, 375–396.

Esam, I., Abdalla, F., Erich, N., and Hermann, M. (2012). Comparison of the groundwater quality in the west Tahta area, upper Egypt in 1989 and 2011. *J. Environ. Prot.* 3, 1442–1457. doi:10.4236/jep.2012.311162

Farrag, A. A. (1982). Hydrogeological studies on the Quaternary water - bearing sediments in the area between Assiut and Aswan. *M. Sc. Thesis. Geol. Dept.*

Gaber, A., Mohamed, A. K., ElGalladi, A., Abdelkareem, M., Beshr, A. M., and Koch, M. (2020). Mapping the groundwater potentiality of west Qena area, Egypt, using integrated remote sensing and hydro-geophysical techniques. *Remote Sens.* 12, 1559. doi:10.3390/rs12101559

Geosoft (2018). *Oasis Montaj (Version 8.4): Software for Processing and Interpretation of Potential-Field Data*. Toronto, ON, Canada: Geosoft Inc. Available at: http://www.geosoft.com (Accessed on October 1, 2018).

Ganoub El-Wadi Petroleum Holding Company (1994). *Geological report of the balyana-1 well*. Cairo, Egypt: The Egyptian General Petroleum Corporation.

Ghazala, H. H., Ibraheem, I. M., Haggag, M., and Lamees, M. (2018a). An integrated approach to evaluate the possibility of urban development around Sohag Governorate, Egypt, using potential field data. *Arab. J. Geosci.* 11 (9), 194–219. doi:10.1007/s12517-018-3535-1

Ghazala, H. H., Ibraheem, I. M., Lamees, M., and Haggag, M. (2018b). Structural study using 2D modeling of the potential field data and GIS technique in Sohag Governorate and its surroundings, Upper Egypt. *NRIAG J. Astron. Geophys.* 7, 334–346. doi:10.1016/j.nrjag.2018.05.008

Griffin, W. R. (1949). Residual gravity in theory and practice. *Geophys J.* 14, 39–56. doi:10.1190/1.1437506

Hemant, K. (2003). "Modelling and interpretation of global lithospheric magnetic anomalies,". Potsdam, Germany: Deutsches GeoForschungsZentrum GFZ. doi:10.48440/GFZ.b103-03109

Hong, H., Tsangaratos, P., Ilia, I., Liu, J., Zhu, A. X., and Chen, W. (2018). Application of fuzzy weight of evidence and data mining techniques in construction of flood susceptibility map of Poyang County, China. *Sci. Total Environ.* 625, 575–588. doi:10.1016/j.scitotenv.2017.12.256

Hunt, C. P., Moskowitz, B. M., and Banerjee, S. K. (1995). "Magnetic properties of rock and minerals," in *Rock physics and phase relation—a handbook of physical constant*. Editor T. J. Ahrens (Washington, DC, USA: American Geophysical Union), 189–204.

Ibraheem, I. M., El-Husseiny, A. A., and Othman, A. A. (2022). Structural and mineral exploration study at the transition zone between the North and the Central Eastern Desert, Egypt, using airborne magnetic and gamma-ray spectrometric data. *Geocarto Int.* 37 (26), 13098–13126. doi:10.1080/10106049.2022.2076915

Ibraheem, I. M., Haggag, M., and Tezkan, B. (2019). Edge detectors as structural imaging tools using aeromagnetic data: a case study of Sohag area. Egypt. *Geosciences* 9 (5), 211. doi:10.3390/geosciences9050211

Ibraheem, I. M., Tezkan, B., Ghazala, H., and Othman, A. A. (2023). A new edge enhancement filter for the interpretation of magnetic field data. *Pure Appl. Geophys.* 180, 2223–2240. doi:10.1007/s00024-023-03249-3

Ikirri, M., Boutaleb, S., Ibraheem, I. M., Abioui, M., Echogdali, F. Z., Abdelrahman, K., et al. (2023). Delineation of groundwater potential area using an AHP, remote sensing, and GIS techniques in the Ifni Basin, Western Anti-Atlas, Morocco. *Water* 15 (7), 1436. doi:10.3390/w15071436

Ismail, E., and El-Rawy, M. (2018). Assessment of groundwater quality in West Sohag, Egypt. *DesalinWater Treat.* 123, 101–108. doi:10.5004/dwt.2018.22687

Issawi, B., Francis, M. H., Youssef, E-S. A. A., and Osman, R. A. (2009). The Phanerozoic Geology of Egypt: A Geodynamic Approach. 2nd edn. Cairo, Egypt: Egyptian Mineral Resources Authority (EMRA).

Jenson, S. K., and Domingue, J. O. (1988). Extracting topographic structure from digital elevation data for geographic information system analysis. *Photogramm. Eng. Remote Sens.* 54, 1593–1600.

Jorge, V. T., Oliveira, S. P., Thanh, L. P., and Duong, V. H. (2023). A balanced edge detector for aeromagnetic data. Vietnam. *J. Earth Sci.* 45, 326–337. doi:10.15625/2615-9783/18461

Lowrie, W. (2007). *Fundamentals of geophysics*. 2nd edn. New York: Cambridge University Press, 381.

Mahmoud, H., and Kotb, A. (2017). Impact of the geological structures on the groundwater potential using geophysical techniques in West Bani Mazar area, El Minia – western Desert, Egypt. *Egypt* 130, 161–173. doi:10.1016/j.jafrearsci.2017.03.024

Mahran, T. M., El-Shater, A., Youssef, A. M., and El-Haddad, B. A. (2013). "Facies analysis and tectonic-climatic controls of the development of Pre-Eonile and Eonile sediments of the Egyptian Nile west of Sohag," in *In the 7th international conference on the geology of Africa*. Assiut, Egypt.

McBridge, E. F., Abdel-Wahab, A., and El-Younsy, A. R. M. (1999). Origin of spheroidal chert nodules, Drunka Formation (lower Eocene), Egypt. *Sedimentology* 46, 733–755. doi:10.1046/j.1365-3091.1999.00253.x

Meijerink, A. M. J., Bannert, D., Batelaan, O., Lubczynski, M., and Pointet, T. (2007) *Remote sensing applications to groundwater; IHP-VI series on groundwater*, 16. Paris, France: United Nations Educational Scientific and Cultural Organization UNESCO.

Melese, T., and Belay, T. (2022). Groundwater potential zone mapping using analytical hierarchy process and GIS in muga watershed, abay basin, Ethiopia. *Glob. Chall.* 6, 2100068. doi:10.1002/gch2.202100068

Meneisy, A. M. (2020). Impact of subsurface structures on groundwater exploration using aeromagnetic and geoelectrical data: a case study at Aswan City, Egypt. *Arab. J. Geosci.* 13, 1213. doi:10.1016/j.ejrs.2020.06.006

Meneisy, A. M., Al Deep, M., and Csámer, A. (2021). Investigation of groundwater potential using magnetic and satellite image data at Wadi El Amal, Aswan, Egypt. *Egypt. J. Remote. Sens. Space. Sci.* 24 (2), 293–309. doi:10.1016/j.ejrs.2020.06.006

Mohamed, H. S. (2021). Structural pattern along the course of the Nile Valley opposite El-Balyana, Upper Egypt, using gravity and magnetic data. *Arabian J. Geosciences* 14, 897. doi:10.1007/s12517-021-07168-2

Mohamed, H. S., and Abu El-Ella, E. (2023). Geophysical investigation on wadi El Assiuti Basin, Eastern Desert, Egypt. *NRIAG J. Astron. Geophys.* 12, 83–95. doi:10.1080/20909977.2023.2230661

Mostafa, H. A. (1979). *Geology of the area northeast of Sohag. M.ScThesis,geology dept*. Egypt: Faculty of Science, Sohag. South Valley University, 259.

Mukherjee, I., and Singh, U. K. (2020). Delineation of groundwater potential zones in a drought-prone semi-arid region of east India using GIS and analytical hierarchical process techniques. *CATENA* 194, 104681 (1-18). doi:10.1016/j.catena.2020.104681

Nabih, N. (2005). Exploratory well data of Egypt (internal report).

Nasuti, Y., Nasuti, A., and Moghadas, D. (2019). STDR: a novel approach for enhancing and edge detection of potential field data. *Pure Appl. Geophys.* 176, 827–841. doi:10.1007/s00024-018-2016-5

Omer, A. A. (1996). *Geological, mineralogical and geochemical studies on the neogene and quaternary nile basin deposits, qena-assiut stretch, Egypt*. Sohag, Egypt: South Valley University. Ph.D. Thesis.

Omran, A. A., Korany, E. A., and Abdel-Rahman, A. A. (2006). "An integrated approach to evaluate groundwater potentiality a case study," in *Proceeding of the 3rd international conference of applied geophysics, 8–20 march Cairo, Egypt*.

Othman, A. A., and Ibraheem, I. M. (2024). Origin of el-maghara anticlines, north Sinai Peninsula, Egypt: insights from gravity data interpretation using edge detection filters. *Arab. J. Sci. Eng.* 49, 863–882. doi:10.1007/s13369-023-08225-6

Patra, H. P., Adhikari, S. K., and Kunar, S. (2016). *Groundwater prospecting and management*. Singapore: Springer.

Pham, L. T., Le-Huy, M., Oksum, E., and Do, T. D. (2018). Determination of maximum tilt angle from analytic signal amplitude of magnetic data by the curvature-based method. Vietnam J. *Earth Sci.* 40, 354–366. doi:10.15625/0866-7187/40/4/13106

Pham, L. T., Oliveira, S. P., Duong, V. H., Abdelrahman, K., Fnais, M. S., Gomez-Ortiz, D., et al. (2023). Aeromagnetic data interpretation of the northern Kontum massif (Vietnam) for mapping subsurface structures. *Geocarto Int.* 38, 1. doi:10.1080/10106049.2023.2246940

Phillips, J. D. (2002). *Processing and interpretation of aeromagnetic data for the santa cruz basin-patagonia mountains area, south-central Arizona*. Washington, DC, USA: US Department of the Interior, US Geological Survey.

Reynolds, J. M. (2011). *An introduction to applied and environmental geophysics*. 2nd ed. West Sussex, UK: John Wiley & Sons.

RIGW (1997). Hydrogeological map of Egypt. *Scale*. 1:100,000; ASRT: Cairo, Egypt.

RIGW (2023). *Groundwater development for irrigation and drainage in the Nile Valley, groundwater development in the area of Sohag, technical note 75, internal report*. Cairo, Egypt: Research Institute for groundwater.

Said, R. (1962). *The geology of Egypt*. Amsterdam, Netherlands: Elsevier, 377p.

Said, R. (1981). *The nile in Egypt. The geological evolution of the River nile*. New York, NY, USA: Springer, 12–92.

Said, R. (1990). *The geology of Egypt*. Rotterdam, Brookfield: Balkema, 731p.

Said, R. (1994). *Origin and evolution of the river nile R. said. The nile: sharing a scarce resource: a historical and technical review of water management and of economical and legal issues*. : University Press.

Seif, E. S. S. A. (2015). Geological evolution of Nile Valley, west Sohag, upper Egypt: a geotechnical perception. *Arab. J. Geosci.* 8, 11049–11072. doi:10.1007/s12517-015-1966-5

Sestini, G. (1984). Tectonic and sedimentary history of the NE African margin (Egypt—Libya). *Geol. Soc. Lond. Spec. Publ.* 17, 161–175. doi:10.1144/gsl.sp.1984.017.01.10

Shebl, A., and Csamer, A. (2021). Stacked vector multi-source lithologic classification utilizing Machine Learning Algorithms: data potentiality and dimensionality monitoring. *Remote Sens. Appl. Soc. Environ.* 24, 100643. doi:10.1016/j.rsase.2021.100643

Shebl, A., Kusky, T., and Csámer, A. (2022). Advanced land imager superiority in lithological classification utilizing machine learning algorithms. *Arab. J. Geosci.* 159 (15), 1–13. doi:10.1007/S12517-022-09948-W

Taloor, A. K., Manhas, D. S., and Kothyari, G. C. (2021). Retrieval of land surface temperature, normalized difference moisture index, normalized difference water index of the Ravi basin using Landsat data. *Appl. Comput. Geosci.* 9, 100051. doi:10.1016/j.acags.2020.100051

Tehrany, M. S., Lee, M. J., Pradhan, B., Jebur, M. N., and Lee, S. (2014). Flood susceptibility mapping using integrated bivariate and multivariate statistical models. *Environ. Earth Sci.* 72, 4001–4015. doi:10.1007/s12665-014-3289-3

Telford, W. M., Geldart, R. E., and Sheriff, R. E. (1990). *Applied geophysics*. 2nd ed. Cambridge, UK: Cambridge University Press.

Thornbury, W. D. (1985). *Principles of geomorphology*. New York, NY, USA; London, UK: John Wiley & Sons.

Thurston, J. B., and Smith, R. S. (1997). Automatic conversion of magnetic data to depth, dip, and susceptibility contrast using the SPI (TM) method. *Geophysics* 62, 807–813. doi:10.1190/1.1444190

Wind, Y., and Saaty, T. L. (1980). Marketing applications of the analytic hierarchy process. *Manag. Sci.* 26, 641–658. doi:10.1287/mnsc.26.7.641

Woodward, J. C., Macklin, M. G., Krom, M. D., and Williams, M. A. (2022). "The River nile: evolution and environment,". Hoboken, NJ, USA: John Wiley & Sons, Ltd., 388–432. doi:10.1002/9781119412632.ch14

Youssef, M. (2003). "Structural setting of central and south Egypt: an overview,", 49: Minoufiya Governate, Egypt: Minoufiya University, 1–13. doi:10.2113/49.suppl_1.1

Youssef, M. I. (1968). Structural pattern of Egypt and its interpretation. *AAPG Bull.* 52, 601–614. doi:10.1306/5d25c44d-16c1-11d7-8645000102c1865d

Zaki, S. R. (2001). *Hydrogeological studies and application of geographic information system for evaluation of water resources and land use projects in southern Sohag Governorate. Msc. Fac. of Science*. Minoufiya University, 179.